Journal of the Mechanics and Physics of Solids 119 (2018) 20–42

Contents lists available at ScienceDirect

Journal of the Mechanics and Physics of Solids

journal homepage: www.elsevier.com/locate/jmps

# A length scale insensitive phase-field damage model for brittle fracture

Jian-Ying Wu[a,*], Vinh Phu Nguyen[b]

[a] State Key Laboratory of Subtropical Building Science, South China University of Technology, Guangzhou 510641, China
[b] Department of Civil Engineering, Monash University, Clayton, Victoria 3800, Australia

ARTICLE INFO

*Article history:*
Received 30 March 2018
Revised 29 May 2018
Accepted 6 June 2018
Available online 13 June 2018

*Keywords:*
Phase-field theory
Length scale
Brittle fracture
Damage
Cohesive zone model

ABSTRACT

Being able to model complex nucleation, propagation, branching and merging of cracks in solids within a unified framework, the classical phase-field models for brittle fracture fail in predicting length scale independent global responses for a solid lacking elastic singularities (e.g., corners, notches, etc.). Motivated from Barenblatt's approximation of Griffith's brittle fracture with a vanishing Irwin's internal length, this paper extends our recent work in quasi-brittle failure (Wu, 2017, 2018a) and presents for the first time a length scale insensitive phase-field damage model for brittle fracture. More specifically, with a set of optimal characteristic functions, a phase-field regularized cohesive zone model (CZM) with linear softening law is addressed and applied to brittle fracture. Both the failure strength and the traction – separation law are independent of the incorporated length scale parameter. Compared to other phase-field models and CZM based discontinuous approaches for brittle fracture, the proposed phase-field regularized CZM is of several merits. On the one hand, being theoretically equivalent to Barenblatt's CZM (at least in the 1-D case), it needs neither the explicit crack representation/tracking nor the elastic penalty stiffness which both are necessary but cumbersome for discontinuous approaches. On the other hand, it gives length scale independent global responses for problems with or without elastic singularities while preserving the expected $\Gamma$-convergence property of phase-field models. Representative numerical examples of several well-known benchmark tests support the above conclusions, validating its capability of modeling both mode-I and mixed-mode brittle fracture.



## 1. Introduction

Fracture is one of the most commonly encountered failure modes of engineering materials and structures. The prevention of cracking induced failure is, therefore, a major concern in engineering designs. Similarly to many other physical phenomena, computational modeling of crack initiation and propagation in solids constitutes an indispensable tool not only to predict the failure of cracked structures but also to shed insights into the failure mechanism of many materials such as concrete, rock, ceramic, metals, biological soft tissues etc.

In the field of fracture mechanics, Griffith's theory (Griffith, 1920) is the momentum work though later developments of e.g., Irwin (1957); Rice (1968), etc., are also noteworthy. Another comparable work is Barenblatt's cohesive zone model (CZM)

* Corresponding author.
*E-mail address:* jywu@scut.edu.cn (J.-Y. Wu).

https://doi.org/10.1016/j.jmps.2018.06.006
0022-5096/

(Barenblatt, 1959) which extends linear elastic fracture mechanics to nonlinear one. Despite its versatility and popularity in both academic and engineering communities, the theory of fracture mechanics, whichever the linear elastic one and the nonlinear one, is intrinsically not self-contained. Extrinsic (sometimes *ad hoc*) criteria have to be introduced to determine when and where a crack nucleates, how much it propagates and in which orientation, and when it branches. Even the above theoretical issues can be solved, intractable numerical challenges present such as the representation of non-smooth crack surfaces and the tracking of crack propagation paths in general 3-D cases.

To remedy the deficiencies of fracture mechanics, Francfort and Marigo (1998) proposed the variational approach to fracture. This groundbreaking theory replaces the stationarity condition in Griffith's energetic approach by a global minimization of the total energy of a cracking solid. Though this modification is conceptually simple, crack initiation and evolution can be quantified with no extra criterion. Later on, motivated from the Ambrosio and Tortorelli (1990) elliptic regularization of the Mumford and Shah (1989) functional in image segmentation, Bourdin et al. (2000) developed the numerically more amenable phase-field model for brittle fracture. Remarkably, complex crack configurations such as multiple crack nucleation, propagation, merging, branching, etc., in general 3-D cases, can be considered within a single framework. Ever since then, a large volume of research efforts have been made in the academic community (Ambati et al., 2015; Bourdin et al., 2008). Recently, the application has been extended from fracture in solids with infinitesimal deformations to plates, shells and composites under finite strains (Areias et al., 2016b; Carollo et al., 2017; Msekh et al., 2018; Reinoso and Paggi, 2017).

In phase-field models, the governing equations, i.e., the conventional equilibrium equation and an extra evolution law of gradient type similar to the screened Poisson equation (Areias et al., 2016a; 2018) for the crack phase-field, are usually derived from the variational approach (Bourdin et al., 2000; 2008). To this end, one has to postulate the total energy functional of a cracking solid. In the case of quasi-static loading, it consists of two parts, i.e., the stored elastic energy of the solid and the dissipated surface energy associated with the crack. As will be briefly reviewed, the later development of phase-field models for fracture mainly roots in postulating appropriate expressions for the above energy functionals.

As far as brittle fracture is concerned, the standard Bourdin et al. (2000) model is isotropic in the sense that it predicts identical tensile and compressive fracture behavior. In order to address asymmetric tensile and compressive (i.e.,the so-called anisotropic) behavior, one common approach is to decompose the stored elastic energy into two parts, one related to tensile fracture and the other to compressive one (the latter is usually neglected). For instance, an anisotropic phase-field model was proposed in Amor et al. (2009) where the volumetric and deviatoric decomposition of the elastic energy density is considered to prevent compressive cracking. Yet another anisotropic model was proposed in Lancioni and Royer-Carfagni (2009) for shear fractures which was applied to cracking in masonry structures. Based on the theory of structured deformation, Freddi and Royer-Carfagni (2010) presented a unified formulation of the Amor et al. (2009); Bourdin et al. (2000) and Lancioni and Royer-Carfagni (2009) models for mode I, mode II, mixed-mode and masonry-like fractures. Miehe et al. (2010b) introduced an intuitive and thermodynamically consistent phase-field formulation in which the spectral decomposition of the strain tensor is used to split the elastic energy. Compared to the mathematically rigorous formulation of Francfort and Marigo (1998) and Bourdin et al. (2000), it is more accessible to the engineering community. Another approach in dealing with asymmetric tensile and compressive behavior is using a hybrid isotropic/anisotropic formulation (Ambati et al., 2015). That is, the stress – strain relation is still given from the stored elastic energy with no split, whereas the phase-field evolution law is associated with a different one, e.g., the one used in those anisotropic phase-field models. Though the hybrid formulation is variationally inconsistent, it is rather flexible in accounting for various failure mechanisms as in Miehe et al. (2015) and Zhang et al. (2017) and is computationally more efficient when the alternating minimization algorithm (Bourdin et al., 2000; 2008) is used.

The above successors of the Bourdin et al. (2000) model are usually referred to as *standard* phase-field models. A common feature is that the sharp crack topology in the dissipated surface energy functional is regularized into a diffuse localization band of infinite support. Consequently, the phase-field governing equation has to be solved in the whole computational domain (Moës et al., 2011). Moreover, except the very rare remedies (Kuhn et al., 2015), these standard phase-field models generally lack the linear elastic stage such that crack nucleation cannot be correctly predicted (Tanné et al., 2018). To address the above issues, Pham et al. (2011a) proposed a *non-standard* phase-field model with a regularized localization band of finite support and a non-zero elastic limit strength. Moreover, the original variational approach to brittle fracture transforms into a stability condition associated with the total energy under the unilateral constraint induced by the irreversibility of the crack phase field (Pham et al., 2011b).

Though phase-field models are very promising for brittle fracture, challenging issues still exist. For instance, for a solid without elastic singularities (e.g., corners, notches etc.,) the existing phase-field models predict crack nucleation at a critical stress inversely proportional to the square root of the length scale parameter. Accordingly, in the limit of a vanishing length scale, the deficiency of Griffith's theory is inherited when dealing with scaling properties and crack nucleation. In order to overcome this issue, it is advocated recently in Amor et al. (2009); Pham et al. (2011a) and Tanné et al. (2018) to regard the length scale parameter as a material property and relate it to the critical stress of the 1-D homogeneous solution; see also Nguyen et al. (2016a) and Pham et al. (2017). If this strategy is adopted, the subtle difference between phase-field models and gradient-damage models (Frémond and Nedjar, 1996; Lorentz and Andrieux, 1999; Pijaudier-Cabot and Burlion, 1996) diminishes. Nevertheless, the $\Gamma$-convergence upon a vanishing length scale favored in the original phase-field model (Bourdin et al., 2000; 2008) is regrettably lost.

Phase-field models for cohesive fracture and quasi-brittle failure are far more under-developed. The first phase-field model for cohesive fracture was set in Bourdin et al. (2008) and further developed in May et al. (2016); Verhoosel and de Borst (2013); Vignollet et al. (2014) and Nguyen et al. (2016b). In the dissipated surface energy functional of these models, Griffith's fracture toughness, usually regarded as a material property, is replaced by a fracture energy function dependent on the crack opening. In order to determine the crack opening, an auxiliary field was introduced (Verhoosel and de Borst, 2013). However, as reported in Verhoosel and de Borst (2013); Vignollet et al. (2014) and May et al. (2016), only crack propagation along pre-defined paths, i.e., interfacial cracks, can be considered. Moreover, the traction continuity condition has to be used as in discontinuous approaches, leading inevitably to stress oscillations around the localization band (Verhoosel and de Borst, 2013). Nguyen et al. (2016b) avoided using the auxiliary field by resorting to the level set method. The resulting model, however, also applies only to material interfaces (or non-propagating cracks).

An alternative approach to model cohesive fracture in phase-field models is using a stored energy functional which depends not only on the displacement and phase fields but also on the incorporated length scale parameter, while the dissipated surface energy functional is the same as that for brittle fracture (Conti et al., 2015; Focardi and Iurlano, 2017; Wu, 2017; 2018a). In this case, the stored elastic energy does not release abruptly, but rather, approaches asymptotically to Griffith's fracture toughness. The crack opening is implicitly expressed in terms of the crack phase field and the introduction of an auxiliary field is no longer needed. In the mathematics community, Conti et al. (2015) proposed a stored energy functional which is proportional to the length scale parameter and proved the $\Gamma$-convergence of the resulting phase-field model to Barenblatt's CZM. However, the numerical examples presented later in Focardi and Iurlano (2017) show that the global responses are also heavily sensitive to the length scale parameter.

Almost at the same time, Wu (2017) proposed a unified phase-field theory for cohesive fracture, characterized by two generic characteristic functions, i.e., the energetic degradation function for the stored elastic energy functional and the geometric crack function for the dissipated surface energy functional. The first optimization condition together with the irreversibility constraint of the crack phase field are employed to derive the governing equations. Later on, an equivalent but much simpler derivation was presented in Wu (2018a) in which only the standard thermodynamics with internal variables is employed. The evolution law for the crack phase field is established based on the energetic equivalence between the sharp crack and the geometrically regularized one, bridging the gap between fracture mechanics and continuum damage mechanics. With two elegantly constructed characteristic functions, a phase-field regularized CZM is established for cohesive cracks. Those popular traction – separation laws (TSL), e.g., the linear, exponential, hyperbolic and Cornelissen et al. (1986) softening curves, etc., can be considered. Extensive numerical examples of quasi-brittle failure (Feng and Wu, 2018; Wu, 2017; 2018a; 2018b) confirm that, the incorporated length scale parameter only affects the localization bandwidth, but it has negligible, if not no, effects on the global responses, so long as the regularized localization band can be sufficiently resolved. As a result, even though it can also be regarded as a material property, the length scale is considered as a numerical parameter of which value can be taken as small as possible. In this way, the $\Gamma$-convergence of the original phase-field model (Bourdin et al., 2000) is preserved with no loss of the length scale independence.

Though the above phase-field regularized CZM is rather generic, so far all the aforesaid work deals with exclusively quasi-brittle failure and brittle fracture has never been considered. We do not know whether it applies to brittle fracture or not, and if it does as expected, what the model parameters should be in order that the global responses are insensitive to the incorporated length scale parameter. Moreover, the relations of this model to other phase-field models for brittle fracture are not clear. The aim of this paper is to make further contributions to the above topics. Motivated from Barenblatt's approximation of Griffith's brittle fracture with a vanishing Irwin's internal length, a length scale insensitive phase-field damage model is for the first time, to the best knowledge of the authors, presented and applied to brittle fracture. Such a phase-field damage model is mostly attractive since it presents a unified approach to deal with both brittle fracture and quasi-brittle failure, while circumventing the deficiencies of other phase-field models and CZM based discontinuous approaches.

The remainder of this paper is structured as follows. Section 2 addresses the proposed phase-field damage model for brittle fracture. The constitutive relations, evolution law and optimal characteristic functions for the phase-field regularized CZM are all presented. Numerical performances of the proposed model are investigated in Section 3. Several representative benchmark tests of brittle fracture under mode-I and mixed-mode failure are numerically analyzed. The most relevant conclusions are drawn in Section 4, closing this paper.

*Notation*. Compact tensor notation is used throughout this paper. As general rules, scalars are denoted by italic light-face Greek or Latin letters (e.g. $a$ or $\lambda$); vectors, second- and fourth-order tensors are signified by italic boldface minuscule, majuscule and blackboard-bold majuscule characters like $\boldsymbol{a}$, $\boldsymbol{A}$ and $\mathbb{A}$, respectively. The inner products with single and double contractions are denoted by '$\cdot$' and ':', respectively.

## 2. Phase-field damage model for brittle fracture

In this section, the length scale insensitive phase-field damage model for brittle fracture is presented. It is motivated from Barenblatt's approximation of Griffith's brittle fracture and based on the unified phase-field damage theory recently developed by the first author (Wu, 2017; 2018a). Its relations to other phase-field models for brittle fracture and to Barenblatt's CZM are also clarified.

The reference configuration of an elastic solid $\Omega \subset \mathbb{R}^{n_{\text{dim}}}$ ($n_{\text{dim}} = 1, 2, 3$) with a set of sharp cracks $\mathcal{S} \subset \mathbb{R}^{n_{\text{dim}}-1}$ is shown in Fig. 1 (left). The external boundary is denoted by $\partial\Omega \subset \mathbb{R}^{n_{\text{dim}}-1}$, with the outward unit normal denoted by vector $\boldsymbol{n}$.

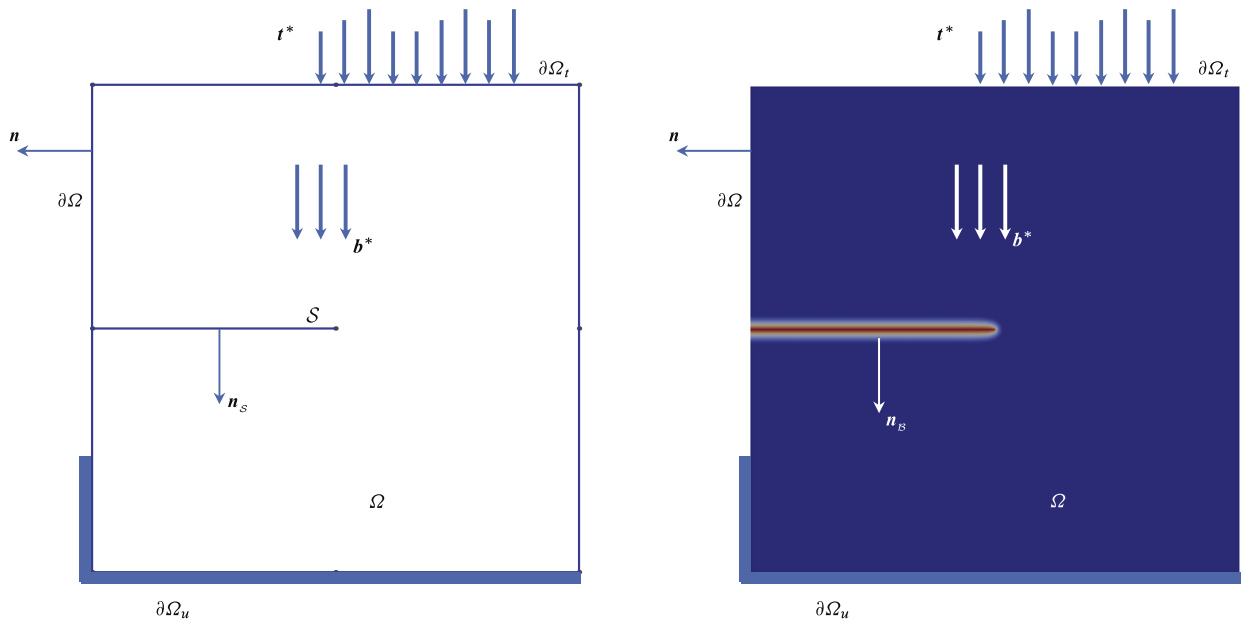


**Fig. 1.** A solid medium with a sharp crack (left) and the phase-field regularization (right).

The material particles of the solid are labeled by their spatial coordinates $\boldsymbol{x}$. The solid is kinematically described by the displacement field $\boldsymbol{u}(\boldsymbol{x}) : \Omega \to \mathbb{R}^{n_{\text{dim}}}$. The infinitesimal strain field $\boldsymbol{\epsilon} : \Omega \to [\mathbb{R}^{n_{\text{dim}} \times n_{\text{dim}}}]^{\text{sym}}$ is given by $\boldsymbol{\epsilon}(\boldsymbol{x}) := \nabla^{\text{sym}} \boldsymbol{u}$, for the symmetric gradient operator $\nabla^{\text{sym}}(\cdot)$ with respect to the spatial coordinate $\boldsymbol{x}$.

Assume that the cracking solid is subjected to specified volumetric body forces (per unit mass) $\boldsymbol{b}^*$ and surface boundary tractions $\boldsymbol{t}^*$ for some part of the external boundary $\partial\Omega_t \subseteq \partial\Omega$. Given displacements $\boldsymbol{u}^*$ are applied to the disjointed remaining boundary $\partial\Omega_u \subseteq \partial\Omega$, i.e., $\partial\Omega_u \cap \partial\Omega_t = \emptyset$ and $\overline{\partial\Omega_u} \cup \overline{\partial\Omega_t} = \partial\Omega$. The classical balance of linear momentum and Neumann boundary condition are expressed as

$$\begin{cases} \nabla \cdot \boldsymbol{\sigma} + \boldsymbol{b}^* = \boldsymbol{0} & \text{in } \Omega \\ \boldsymbol{\sigma} \cdot \boldsymbol{n} = \boldsymbol{t}^* & \text{on } \partial\Omega_t \end{cases} \tag{2.1}$$

where the stress tensor $\boldsymbol{\sigma}$ conjugated to the strain field $\boldsymbol{\epsilon}$ is determined from a specific constitutive model, e.g., the phase-field damage model that follows.

### 2.1. Barenblatt's approximation of Griffith's brittle fracture

A fundamental ingredient of phase-field models for fracture is the characterization of the dissipated surface energy during crack propagation. In Griffith's theory for brittle fracture, the energy amount dissipated throughout the failure process is proportional to the area of the crack surface, i.e.,

$$\mathscr{D} = G_{\text{f}} A_{\mathcal{S}} = G_{\text{f}} \int_{\mathcal{S}} \mathrm{d}A \tag{2.2}$$

where $A_{\mathcal{S}}$ represents the surface area of the sharp crack $\mathcal{S}$; the proportionality factor, denoted by $G_{\text{f}}$, is the fracture toughness or energy, usually regarded as a material property; see Fig. 2(a). Being the macroscopic manifestation of the energy spent through the microscopic breaking of inter-atomic bonds, the dissipated energy functional (2.2) holds only if inter-atomic bonding is ruled by a Lennard-Jones type interaction potential (Bourdin et al., 2008). However, this is usually not the case, and inter-atomic bonds of the underlying lattice of an crystalline solid will stretch before they break. This results in some degree of reversibility around the crack tip preceding the advance of a crack. In other words, there is a barrier for bonds to break, which can be regarded as the elastic part of the underlying inter-atomic potential.

The above consideration has prompted the replacement of Griffith's surface energy by Barenblatt's counterpart of the following form

$$\mathscr{D} = G_{\text{f}} A_{\mathcal{S}} \approx \int_{\mathcal{S}} \mathcal{G}(w) \, \mathrm{d}A \tag{2.3}$$

where Barenblatt's fracture energy function $\mathcal{G}(\cdot)$ depends on the maximum value $w$ of the crack opening. The concave and monotonically increasing function $\mathcal{G}(\cdot)$ takes the value 0 at $w = 0$ and asymptotically converges to the fracture

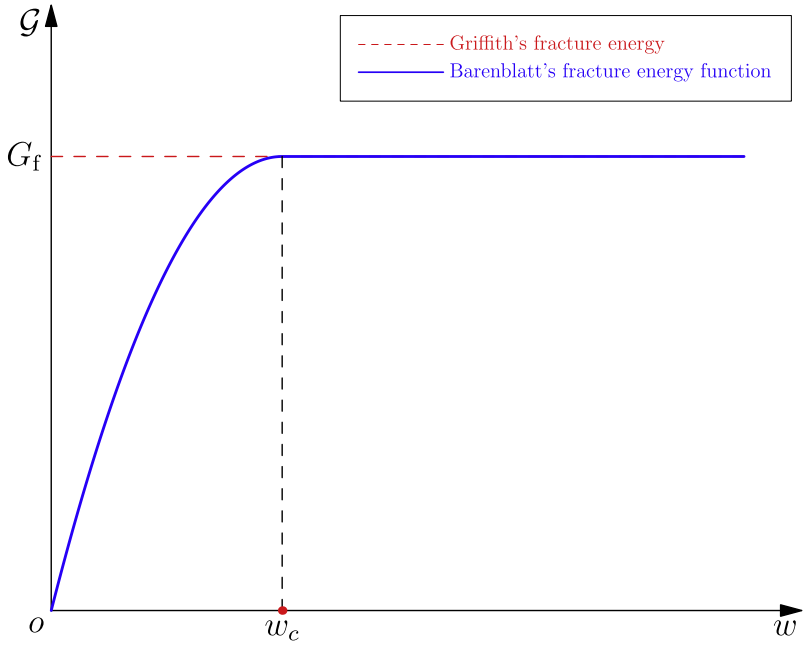


(a) Fracture toughness *versus* fracture energy function

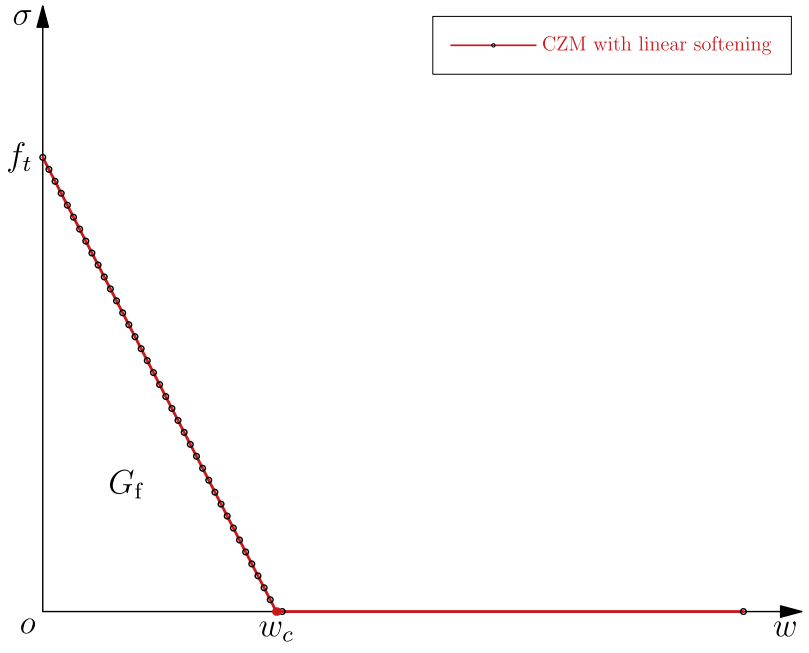


(b) Linear traction – separation law

**Fig. 2.** Barenblatt's CZM (Barenblatt, 1959) approximation of Griffith's (Griffith, 1920) brittle fracture.

toughness $G_{\mathrm{f}}$

$$\mathcal{G}(0) = 0, \qquad \lim_{w\to\infty} \mathcal{G}(w) = G_{\mathrm{f}} \tag{2.4}$$

It then allows defining the cohesive traction $t \in (0, +\infty)$ (the stress $\sigma$ in the 1-D case) across the crack surface as the slope of the fracture energy function $\mathcal{G}(w)$, i.e.,

$$t = \frac{\partial \mathcal{G}}{\partial w} \tag{2.5}$$

which is always positive and finite, with the value at $w = 0$ denoted by the failure strength $f_t$. Note that in Griffith's theory the fracture energy $G_{\mathrm{f}}$ is instantly dissipated upon the creation of a unit fracture surface and the resulting failure strength is infinite. Contrariwise, in Barenblatt's CZM the energy is released gradually in accordance with the fracture energy function $\mathcal{G}(w)$, resulting in a cohesive traction $t(w)$ decaying from the finite failure strength $f_t$ to zero.

In particular, let us consider the simplest linear softening curve shown in Fig. 2(b)

$$\sigma(w) = f_t \max\left(1 - \frac{f_t}{2G_{\mathrm{f}}} w, 0\right) \tag{2.6}$$

with the initial slope $k_0$ and ultimate crack opening $w_c$ given by

$$k_0 = -\frac{f_t^2}{2G_{\mathrm{f}}}, \qquad w_c = \frac{2G_{\mathrm{f}}}{f_t} \tag{2.7}$$

The associated fracture energy function $\mathcal{G}(w)$ is depicted by the solid line in Fig. 2(a).

As both fracture toughness $G_{\mathrm{f}}$ and failure strength $f_t$ are independent material properties, having different dimensions (SI units: J/m$^2$ and N/m$^2$, respectively), the so-called Irwin's internal length $l_{\mathrm{ch}}$ is usually introduced to characterize the size of the fracture process zone (FPZ) ahead of a crack tip

$$l_{\mathrm{ch}} := \frac{E_0 G_{\mathrm{f}}}{f_t^2} \tag{2.8}$$

For a vanishing internal length $l_{\mathrm{ch}} \to 0$, one has $f_t \to \infty$, $k_0 \to -\infty$ and $w_c \to 0$. In this case, Griffith's brittle fracture is asymptotically recovered; see Giacomini (2005) for the mathematical proof. Therefore, Barenblatt's CZM can be used not only for cohesive fracture, but also for brittle one. The above fact motivates the phase-field regularized CZM for brittle fracture presented later in this work.

**Remark 2.1.** In the numerical implementation of CZM based discontinuous approaches, one usually has to represent the crack surface (Duflot, 2007) and track the crack propagation path (Dumstorff and Meschke, 2007). Another drawback is that an elastic penalty stiffness, or the dummy stiffness, usually has to be introduced to prevent compressive contacts (Unger et al., 2007). □

### 2.2. Unified phase-field damage theory

In the literature, Bourdin et al. (2008) adopted Barenblatt's surface energy (2.3) to develop a phase-field model for cohesive fracture. This model was further elaborated in May et al. (2016); Verhoosel and de Borst (2013); Vignollet et al. (2014) and Nguyen et al. (2016b) with the introduction of an extra axillary field variable. However, such a model only applies to cracks propagating along pre-defined paths or material interfaces. Recently, the first author (Wu, 2017; 2018a) proposed a unified phase-field damage theory for cohesive fracture, though other models for brittle one can be recovered as particular examples. Remarkably, the formal expressions for the stored and dissipated energy functionals in the original phase-field model (Bourdin et al., 2000) are preserved. In particular, the dissipated surface energy functional is still expressed in terms of Griffith's fracture toughness. In this section the above unified phase-field damage theory is briefly recalled.

#### 2.2.1. Geometric regularization of sharp cracks

In the context of phase-field models for fracture (Bourdin et al., 2000; 2008; Miehe et al., 2010a; Pham et al., 2011a; Wu, 2017; 2018a), the sharp crack $\mathcal{S}$ is smeared over a localization band $\mathcal{B} \subseteq \Omega$ in which the diffuse phase-field or damage field $d(\boldsymbol{x}) : \mathcal{B} \to [0, 1]$ localizes, with the exterior domain $\Omega \backslash \mathcal{B}$ being intact; see Fig. 1 (right) for an illustration. The damage irreversibility reads $\dot{d} \geq 0$, with $\dot{(\,)}$ being the time derivative. Note that Dirichlet boundary conditions, e.g., $d(\boldsymbol{x}) = 0$ for elastic domains and $d(\boldsymbol{x}) = 1$ for pre-defined cracks can also be considered as well; see Wu (2017, 2018a) for the details.

Being a fundamental ingredient of any phase-field damage model, the sharp crack surface $A_{\mathcal{S}}$ is geometrically regularized by the following phase-field approximation $A_d(d)$

$$\underbrace{A_{\mathcal{S}} = \int_{\mathcal{S}} \mathrm{d}A}_{\text{sharp crack}} \approx \underbrace{\int_{\mathcal{B}} \gamma(d)\, \mathrm{d}V = A_d(d)}_{\text{regularized crack}} \tag{2.9}$$

for the crack surface density functional $\gamma(d)$

$$\gamma(d) = \frac{1}{c_0}\left[\frac{1}{b}\alpha(d) + b\left|\nabla d\right|^2\right] \qquad \text{with} \qquad c_0 = 4\int_0^1 \sqrt{\alpha(\beta)}\,\mathrm{d}\beta \tag{2.10}$$

where $b$ is a length scale characterizes the localization bandwidth; the geometric crack function $\alpha(d) \in [0, 1]$, satisfying the properties that $\alpha(d) = 0$ for $d = 0$ and $\alpha(d) = 1$ for $d = 1$, determines the ultimate distribution of the crack phase field (Wu, 2017). The crack surface density function (2.10) is motivated from the elliptic regularization (Ambrosio and Tortorelli, 1990) of the Mumford–Shah functional (Mumford and Shah, 1989) for image segmentation. More specifically, for a vanishing length scale $b \to 0$ the sharp crack topology $A_s$ is recovered in the context of the $\Gamma$-convergence theorem (Braides, 1998)

$$A_s = \lim_{b\to 0} A_d(d) \tag{2.11}$$

In the literature of phase-field models it is becoming more and more popular that the length scale parameter is interpreted as a material property; see Pham et al. (2011a) and Tanné et al. (2018) among many others, at the cost of losing the $\Gamma$-convergence of the original phase-field model (Bourdin et al., 2000; 2008). In this work, an alternative approach is adopted to address the issue of length scale dependence while preserving the $\Gamma$-convergence.

*2.2.2. Constitutive relations and damage evolution law*

For a cracking solid with the local free energy density $\psi(\boldsymbol{\epsilon}, d)$, the stress–strain relation reads

$$\boldsymbol{\sigma} := \frac{\partial}{\partial \boldsymbol{\epsilon}}\psi(\boldsymbol{\epsilon}, d) \tag{2.12a}$$

for the stress tensor $\boldsymbol{\sigma}$ conjugate to the strain field $\boldsymbol{\epsilon}$. The specific expression of the free energy $\psi$ will be given later. The associated damage energy release rate (driving force) $Y$ is given by

$$Y := -\frac{\partial}{\partial d}\psi(\boldsymbol{\epsilon}, d) = -\omega'(d)\bar{Y} \qquad \text{with} \qquad \bar{Y} := \frac{\partial \psi}{\partial \omega} \tag{2.12b}$$

where the *effective* damage driving force $\bar{Y}$ is conjugate to an appropriate energetic degradation (monotonically non-increasing) function $\omega(d)$: $[0, 1] \to [1, 0]$ of the damage variable $d$, with $\omega'(d) = \partial\omega/\partial d \le 0$ being the first derivative.

In most of the existing phase-field damage models the damage evolution law is usually derived from variational or thermodynamical arguments (Bourdin et al., 2000; Miehe et al., 2010a; Wu, 2017). Alternatively, Wu (2018a) proposed using the following *postulate of energetic equivalence* between the dissipation rates due to the evolution of the localization band $\mathcal{B}$ and of the original sharp crack $\mathcal{S}$, i.e.

$$\dot{\mathscr{D}} = \underbrace{G_{\mathrm{f}}\dot{A}_s}_{\text{sharp crack}} \approx \underbrace{G_{\mathrm{f}}\int_{\mathcal{B}} \dot{\gamma}(d)\,\mathrm{d}V}_{\text{regularized crack}} = \int_{\mathcal{B}} Y\,\dot{d}\,\mathrm{d}V \ge 0 \tag{2.13}$$

Note again that Griffith's fracture toughness is used in the energy dissipation rate (2.13).

Applying the divergence theorem to the *postulate of energetic equivalence* (2.13) and calling for the dissipative nature of damage evolution (i.e., $\dot{d} \ge 0$), yield the following damage criterion (Wu, 2018a)

$$g(Y, d) := Y - G_{\mathrm{f}}\,\delta_d\gamma \begin{cases} = 0 & \dot{d} > 0 \\ < 0 & \dot{d} = 0 \end{cases} \tag{2.14a}$$

and the boundary condition of Neumann-type

$$\nabla d \cdot \boldsymbol{n}_{\mathcal{B}} = 0 \qquad \text{on } \partial\mathcal{B} \tag{2.14b}$$

where $\boldsymbol{n}_{\mathcal{B}}$ is the outward unit normal vector of the boundary $\partial\mathcal{B}$; the variational derivative $\delta_d\gamma$ of the crack surface density functional (2.10) is expressed as

$$\delta_d\gamma := \partial_d\gamma - \nabla\cdot\left(\partial_{\nabla d}\gamma\right) = \frac{1}{c_0}\left[\frac{1}{b}\alpha'(d) - 2b\Delta d\right] \tag{2.15}$$

for the Laplacian $\Delta d = \nabla\cdot\nabla d$ and the first derivative $\alpha'(d) := \partial\alpha/\partial d$. Note that the presence of Lapalacian $\Delta d$ guarantees the well-posedness of the resulting (initial) boundary value problem.

**Remark 2.2.** The damage criterion (2.14a) can be rewritten as the following Karush–Kuhn–Tucker loading/unloading conditions (Wu, 2017; 2018a)

$$\dot{d} \ge 0, \qquad g(Y, d) \le 0, \qquad \dot{d}g(Y, d) \equiv 0 \qquad \text{in } \mathcal{B} \tag{2.16}$$

for rate-independent materials. □

**Remark 2.3.** The crack phase field vanishes at the boundary of the localization band. However, the precise locations of the localization band and of the boundary are neither known *a priori* nor fixed all along. Accordingly, despite their physical meaningfulness, such Dirichlet boundary conditions make no sense in the proposed model. Contrariwise, similarly to

the traction boundary condition $(2.1)_2$, the Neumann boundary condition (2.14b) for the crack phase-field is intrinsically enforced in the weak form in the numerical implementation. This property is very important for automatically determining the *a priori* unknown localization band from the momentum balance equation $(2.1)_1$ and the phase-field evolution law (2.14a). □

### 2.3. Phase-field regularized cohesive zone model (CZM)

In this section, the above unified phase-field damage theory is particularized for cohesive fracture, resulting in a phase-field regularized CZM with linear softening law.

#### 2.3.1. A hybrid phase-field formulation

As the simplest case, the free energy density function $\psi(\boldsymbol{\epsilon}, d)$ is defined as the initial strain energy $\psi_0(\boldsymbol{\epsilon})$ deteriorated isotropically by the energetic degradation function $\omega(d)$, i.e,

$$\psi(\boldsymbol{\epsilon}, d) = \omega(d)\psi_0(\boldsymbol{\epsilon}), \qquad \psi_0(\boldsymbol{\epsilon}) = \frac{1}{2}\boldsymbol{\epsilon} : \mathbb{E}_0 : \boldsymbol{\epsilon} = \frac{1}{2}\bar{\boldsymbol{\sigma}} : \mathbb{C}_0 : \bar{\boldsymbol{\sigma}} \tag{2.17}$$

where the effective stress tensor $\bar{\boldsymbol{\sigma}}$ is defined by the elastic relation $\bar{\boldsymbol{\sigma}} = \mathbb{E}_0 : \boldsymbol{\epsilon}$, with $\mathbb{E}_0$ and $\mathbb{C}_0$ being the elastic stiffness and compliance tensors, respectively. It then follows from the constitutive relations (2.12) that

$$\begin{cases} \boldsymbol{\sigma} := \dfrac{\partial \psi}{\partial \boldsymbol{\epsilon}} = \omega(d)\bar{\boldsymbol{\sigma}} & \text{with} \quad \bar{\boldsymbol{\sigma}} = \dfrac{\partial \psi_0}{\partial \boldsymbol{\epsilon}} = \mathbb{E}_0 : \boldsymbol{\epsilon} \\ Y := -\dfrac{\partial \psi}{\partial d} = -\omega'(d)\bar{Y} & \text{with} \quad \bar{Y} = \dfrac{\partial \psi}{\partial \omega} = \dfrac{1}{2}\,\bar{\boldsymbol{\sigma}} : \mathbb{C}_0 : \bar{\boldsymbol{\sigma}} \end{cases} \tag{2.18}$$

The resulting isotropic phase-field damage model predicts identical tensile and compressive fracture behavior.

In order to address the above issue, an anisotropic formulation with tension/compression split can be considered as in Amor et al. (2009); Miehe et al. (2010a); Wu and Cervera (2018) and Lancioni and Royer-Carfagni (2009). However, the split makes the displacement subproblem nonlinear in the framework of staggered or alternating minimization solvers and brings about extra computational costs. In this work, the so-called hybrid model (Ambati et al., 2015; Wu, 2017; 2018a) is considered. That is, the stress $\boldsymbol{\sigma}$ is still associated with the free energy function (2.17), while a different one is postulated for the damage driving force $Y$, i.e.,

$$\bar{\psi}(\boldsymbol{\epsilon}, d) = \omega(d)\bar{\psi}_0(\boldsymbol{\epsilon}), \qquad \bar{\psi}_0(\boldsymbol{\epsilon}) = \frac{1}{2E_0}\langle\bar{\sigma}_1\rangle^2 \tag{2.19}$$

where $\bar{\sigma}_1$ denotes the major principle value of the effective stress $\bar{\boldsymbol{\sigma}}$; Macaulay brackets $\langle\cdot\rangle$ are defined as $\langle x\rangle = \max\{x, 0\}$. Compared to the formulation in Wu (2017, 2018a), the Rankine criterion for tension-dominated failure is employed here. The resulting constitutive relations are then given by

$$\begin{cases} \boldsymbol{\sigma} := \dfrac{\partial \psi}{\partial \boldsymbol{\epsilon}} = \omega(d)\bar{\boldsymbol{\sigma}} & \text{with} \quad \bar{\boldsymbol{\sigma}} = \dfrac{\partial \psi_0}{\partial \boldsymbol{\epsilon}} = \mathbb{E}_0 : \boldsymbol{\epsilon} \\ Y := -\dfrac{\partial \bar{\psi}}{\partial d} = -\omega'(d)\bar{Y} & \text{with} \quad \bar{Y} = \dfrac{\partial \bar{\psi}}{\partial \omega} = \dfrac{1}{2E_0}\langle\bar{\sigma}_1\rangle^2 \end{cases} \tag{2.20}$$

Note that the hybrid model is no longer variationally consistent. However, such a variational crime does not violate the second law of thermodynamics; see Remark 2.4.

The above hybrid isotropic/anisotropic formulation consists of an isotropic constitutive relation for the stress and an anisotropic evolution law for the phase field. It is able to capture asymmetric tensile and compressive behavior typically for brittle fracture while preserving the linearity of the displacement subproblem.

**Remark 2.4.** For the free energy function (2.17), the first and second laws of thermodynamics in global form give

$$\dot{\mathscr{D}} = \int_\Omega \Big[ -\omega'(d)\psi_0(\boldsymbol{\epsilon}) \Big]\dot{d}\, \mathrm{d}V \geq 0 \tag{2.21}$$

The above energy dissipation inequality holds for any monotonically non-increasing energetic degradation function $\omega(d)$ satisfying $\omega'(d) \leq 0$. □

#### 2.3.2. Generic characteristic functions

The above hybrid phase-field damage model is characterized by two characteristic functions namely, the geometric crack function $\alpha(d)$ regularizing the sharp crack topology and the energetic degradation function $\omega(d)$ defining the free energy density potential.

In accordance with Wu (2017), the following generic expressions are considered

$$\alpha(d) = d \cdot \phi(d), \qquad \omega(d) = \frac{\big(1-d\big)^p}{\big(1-d\big)^p + a_1 d \cdot P(d)} \tag{2.22a}$$

for the polynomials $\phi(d)$ and $P(d)$

$$\phi(d) = \xi + \big(1-\xi\big)d, \qquad P(d) = 1 + a_2 d + a_2 a_3 d^2 + \cdots \tag{2.22b}$$

where the constant $\xi \in (0, 2]$, the exponent $p \geq 2$, and the coefficients $a_1 > 0, a_2, a_3, \ldots,$ are all parameters to be determined. Note that the standard phase-field model (Bourdin et al., 2000; 2008) with $\xi = 0$ is not further discussed in this work since it lacks an initial elastic domain.

*2.3.3. 1-D analytical results*

In order to gain insights into the above phase-field damage model and clarify its relation to Barenblatt's CZM, we present the 1-D analytical results. In this case, the stress $\sigma$ and the damage driving force $Y$ are given from Eq. (2.18) or (2.20), i.e.,

$$\sigma = \omega(d) E_0 \epsilon, \qquad Y = -\omega'(d)\frac{1}{2}E_0\epsilon^2 \tag{2.23}$$

for Young's modulus $E_0$ of the material.

Let us consider a bar $x \in [0, L]$ which is long enough such that the crack evolution is not affected by boundary effects. The left end of the bar is fixed while the right end is stretched by an increasing displacement $u^*$ along axis $x$. The distributed body forces $\boldsymbol{b}^*$ are neglected such that stress $\sigma(x)$ is uniformly distributed along the whole bar. It is assumed that the crack is initiated at any interior point $x = x_0$ and the localization band is localized in the domain $\mathcal{B} := [x_0 - D, x_0 + D]$, with $D \ll L$ being the half bandwidth. By recalling the constitutive relations (2.23) the displacement $u^*$ is given by

$$u^*(\sigma) = \int_0^L \epsilon(\sigma)\, \mathrm{d}x = \frac{\sigma}{E_0}\int_0^L \omega^{-1}(d(x))\, \mathrm{d}x = \frac{\sigma}{E_0}L + w(\sigma) \tag{2.24}$$

where, in the most right hand side, the first term is the elastic displacement of the entire bar, and the second one represents the extra contribution due to the crack opening, expressed as

$$w(\sigma) := \frac{\sigma}{E_0}\int_{-D}^{D}\Big[\omega^{-1}(d(x+x_0)) - 1\Big]\,\mathrm{d}x = \frac{2\sigma}{E_0}\int_0^D \Big[\omega^{-1}(d(x+x_0)) - 1\Big]\,\mathrm{d}x \tag{2.25}$$

Therefore, provided the cracking opening $w(\sigma)$ is independent of the length scale parameter $b$, the proposed phase-field regularized CZM converges to Barenblatt's CZM as expected.

After some cumbersome but straightforward algebraic manipulations, the softening curve $\sigma(w)$, parametrized by the maximum damage $d^* \in [0, 1]$ at the centroid of the localization band, is given by (Wu, 2017)

$$\sigma(d^*) = \sigma_c\sqrt{\frac{\phi(d^*)\big(1-d^*\big)^p}{\xi P(d^*)}} \tag{2.26a}$$

$$w(d^*) = \frac{4G_f\sqrt{\xi}}{c_0\sigma_c}\int_0^{d^*}\Big[\frac{P(d^*)}{\phi(d^*)\big(1-d^*\big)^p}\cdot\phi(\hat{d}) - \frac{P(\hat{d})}{\big(1-\hat{d}\big)^p}\Big]^{-\frac{1}{2}}\frac{\sqrt{\hat{d}}\cdot P(\hat{d})}{\big(1-\hat{d}\big)^p}\mathrm{d}\hat{d} \tag{2.26b}$$

where the critical stress $\sigma_c$ is expressed as

$$\sigma_c = \sqrt{\frac{2\xi E_0 G_f}{c_0 a_1 b}} \tag{2.27}$$

Note that the closed-form expression $\sigma(w)$ is only possible for some very particular cases, e.g., the linear softening law considered in this work.

For the softening curve (2.26), the initial slope $k_0$ and the ultimate jump $w_c$ are given in Eqs. (A.1) from which the coefficients $a_2$ and $a_3$ in the polynomial $P(d)$ are calibrated as in Eqs. (A.2). Moreover, the initial half bandwidth $D_0(\xi, k_0)$ and the ultimate one $D_u(\xi)$ are expressed as in Eqs. (A.3), with the former dependent on the initial slope $k_0$ of a given softening curve $\sigma(w)$ as well as on the parameter $\xi \in (0, 2]$.

*2.3.4. Griffith's brittle fracture* versus *Barenblatt's CZM*

If the parameter $a_1 > 0$ is fixed, i.e.,independent of the length scale $b$, it follows from the relations (2.27) and (A.1) that

$$\sigma_c \propto b^{-1/2} \to \infty, \qquad k_0 \propto -b^{-1} \to -\infty, \qquad w_c \propto b^{1/2} \to 0 \tag{2.28}$$

for a vanishing length scale $b \to 0$. Accordingly, if the length scale $b$ is regarded as a numerical parameter that can be as small as possible, brittle fracture in the context of Griffith's theory is recovered. For instance, let us consider the following quadratic energetic degradation function

$$\omega(d) = \big(1-d\big)^2 \qquad \Longleftrightarrow \qquad p = 2, \quad a_1 = 2, \quad a_2 = -\frac{1}{2}, \quad a_3 = 0 \tag{2.29}$$

In this case, the critical stress $\sigma_c$ is given by

$$\sigma_c = \begin{cases} \sqrt{\dfrac{3E_0G_{\rm f}}{8b}} & \alpha(d) = d \\ \sqrt{\dfrac{2E_0G_{\rm f}}{\pi b}} & \alpha(d) = 2\ d - d^2 \end{cases} \tag{2.30}$$

Compared to the standard phase-field models (Bourdin et al., 2000; 2008; Miehe et al., 2010a) with $\xi = 0$, crack nucleates only if the critical stress $\sigma_c > 0$ is reached. However, for a solid lacking an elastic singularity, the critical stress when a crack nucleates is inversely proportional to the square root of the length scale parameter, inheriting the intrinsic deficiency of Griffith's theory (Tanné et al., 2018).

To address the above issue, one can treat the critical stress $\sigma_c$ as an intrinsic material property i.e.,the failure strength $f_t$. It then follows from the relation (2.27) that

$$\sigma_c = \sqrt{\frac{2\xi E_0G_{\rm f}}{c_0a_1b}} = f_t \qquad \Longrightarrow \qquad ba_1 = \frac{2\xi E_0G_{\rm f}}{c_0f_t^2} = \frac{2\xi}{c_0}l_{\rm ch} \tag{2.31}$$

That is, crack nucleates when the failure strength $f_t$ is reached. In this context, regarding the length scale parameter $b$, the following two cases can be discussed:

- On the one hand, the length scale parameter $b$ is regarded as a material property and is proportional to the Irwin's internal length $l_{\rm ch}$ i.e.,

$$b = \frac{2\xi}{a_1c_0}l_{\rm ch} \tag{2.32}$$

  In this case, the parameter $a_1$ is a constant as well for a given parameter $\xi \in (0, 2]$. For instance, regarding the quadratic energetic degradation function (2.29) i.e., $a_1 = 2$, one has the following results

$$b = \begin{cases} \dfrac{3}{8}l_{\rm ch} & \alpha(d) = d \\ \dfrac{2}{\pi}l_{\rm ch} & \alpha(d) = 2d - d^2 \end{cases} \tag{2.33}$$

  This strategy was first advocated by Pham et al. (2011a) for $\alpha = d$ and then adopted in Nguyen et al. (2016a) and Pham et al. (2017) for the standard phase-field model with $\alpha(d) = d^2$; see also Tanné et al. (2018). However, the length scale parameter so determined is generally not small enough to resolve the regularized crack surface, resulting in an over-estimation of the dissipated surface energy.
- On the other hand, the length scale $b$ is regarded as a numerical parameter that can be as small as possible, resulting in an inversely proportional parameter $a_1$ i.e.,

$$a_1 = \frac{2\xi}{c_0b}l_{\rm ch} \tag{2.34}$$

  In this case, though the energetic degradation function (2.22) also depends on the incorporated length scale parameter, both the failure strength (2.27) and the softening law (2.26) are independent of it. This property allows defining a general traction – separation law in the context of Barenblatt's CZM (Barenblatt, 1959; Hillerborg et al., 1976). Consequently, global responses insensitive to the length scale $b$ can be guaranteed, so long as the sharp crack surface $A_\mathcal{S}$ is sufficiently approximated by the regularized counterpart $A_d$ as in Eq. (2.9). This fact is in sharp contrast to those phase-field models of which the numerical predictions heavily depend on the length scale parameter.

*2.3.5. Optimal characteristic functions for CZM with linear softening law*

For the linear softening law (2.6), the ultimate crack opening $w_c$ is positive and finite, corresponding to the parameter $p = 2$. Moreover, the crack irreversibility condition $\dot{d} \geq 0$ implies that the localization band has to be non-shrinking (otherwise, the damage in the shrunk domain would decease), i.e.,

$$\dot{d} \geq 0 \qquad \Longrightarrow \qquad \dot{D} \geq 0 \qquad \Longrightarrow \qquad D_0(\xi, k_0) \leq D_u(\xi) \tag{2.35}$$

for the initial slope $k_0$ in Eq. $(2.7)_1$. It then follows from the relations (A.3) that

$$\xi = 2, \qquad D_0 = D_u = \frac{\pi}{2}b \tag{2.36}$$

That is, *if and only if* $\xi = 2$, can the CZM with the linear softening curve (2.6) be reproduced by a phase-field damage model, and in this case the localization bandwidth $D$ is fixed as $\frac{1}{2}\pi b$ all along. Otherwise, strict conditions have to be enforced as e.g.,in Lorentz (2017), on the involved model parameters for any other parameter $\xi \in (0, 2)$.

For the parameters $\xi = 2$ (i.e.,$c_0 = \pi$) and $p = 2$, it follows from the relations (2.34) and (A.2) that

$$a_1 = \frac{4}{\pi b} l_{\rm ch}, \qquad a_2 = -\frac{1}{2}, \qquad a_3 = 0 \tag{2.37}$$

and the optimal characteristic functions (2.22) become

$$\alpha(d) = 2\,d - d^2 = 1 - \big(1-d\big)^2 \tag{2.38a}$$

$$\omega(d) = \frac{\big(1-d\big)^2}{\big(1-d\big)^2 + a_1 d \cdot \big(1 - \frac{1}{2} d\big)} \tag{2.38b}$$

where the parameter $a_1 > 0$ is determined by the relation $(2.37)_1$. For the convexity of the energetic degradation function (2.38b) and of the resulting free energy functional (2.17), the length scale $b$ should satisfy

$$a_1 \geq \frac{3}{2} \qquad \Longleftrightarrow \qquad b \leq \frac{8}{3\pi} l_{\rm ch} \approx 0.85 l_{\rm ch} \tag{2.39}$$

As it is necessary to consider a small length scale parameter $b \ll l_{\rm ch}$ in order to sufficiently resolve the phase-field regularization (2.9), the above upper bound to the length scale $b$ is almost useless. Note that the classical quadratic polynomial $\omega(d) = (1-d)^2$ is a particular case of the generic one (2.38b) with $a_1 = 2$ and $b = 2l_{\rm ch}/\pi$. However, only together with the geometric crack function (2.38a) can the linear softening curve be reproduced.

For the optimal constitutive functions (2.38), the traction – separation law $\sigma(w)$ defined in Eqs. (2.26) recover the linear softening curve (2.6), i.e.,

$$\sigma(d^*) = \big(1 - d^*\big) f_t, \qquad w(d^*) = \frac{2G_{\rm f}}{f_t} d^* \tag{2.40}$$

for the maximum damage $d^* \in [0,\, 1]$. Remarkably, for various values of the length scale parameter $b$, though the energetic degradation functions differ, the predicted softening laws coincide with the linear one; see Fig. 3.

**Remark 2.5.** the above linear traction – separation law is implicitly characterized by the evolution of the crack phase-field. The resulting phase-field regularized CZM needs neither the elastic penalty (or dummy) stiffness nor the crack tracking strategy as in CZM based discontinuous approaches. □

## 3. Numerical examples

In this section several representative numerical examples are presented to demonstrate the performance of the proposed phase-field regularized CZM. In the numerical implementation, the governing equations (2.1) and (2.14) are numerically discretized by the multi-field finite element method. The resulting system of nonlinear equations are solved by the alternating minimization algorithm (Bourdin et al., 2000; 2008). In particular, the indirect displacement control (de Borst, 1987) is used to track the unstable post-peak behavior, whereas the damage subproblem is solved by the bound-constrained optimization solver incorporated in the toolkit PETSc (Balay et al., 2016); see Wu (2018b) for the details.

In the context of phase-field models, the length scale needs to be resolved by sufficiently fine spatial discretization. If not explicitly specified, a finer level of finite element discretization are considered within the sub-domain encompassing potential crack paths in order to relieve computational burdens. From our previous experiences, the mesh size $h = \big(\frac{1}{10} \sim \frac{1}{5}\big) b$ is usually enough in these refined sub-domains. Unstructured and uniform piece-wise linear triangular elements, generated by the software `gmsh` (Geuzaine and Remacle, 2009) without any interference, are used to discretize the computational domains. In all examples, the plane stress state is assumed.

### 3.1. Uniaxial traction of a softening bar

A bar of length $L = 200$ mm, of height $H = 10$ mm and of unit out-of-plane thickness under uniaxial traction is first considered. As shown in Fig. 4, the left edge of the bar is fixed, while the right edge is stretched by a monotonically increasing displacement.

The following material properties are assumed: Young's modulus $E_0 = 3.0 \times 10^4$ MPa, Poisson's ratio $\nu_0 = 0.2$ and the fracture energy $G_{\rm f} = 0.008$ N/mm. Two length scale parameters, $b = 10$ mm and $b = 5$ mm, respectively, are considered. For each length scale, uniformly distributed unstructured finite elements of average size $h = b/10$ are used to resolve the damage field of high gradient. As shown in Wu (2017), if no Dirichlet condition is imposed on the crack phase-field, the localization band may form at either of the boundary edges, dependent on numerical errors (Pham et al., 2011a). In order to avoid such a case, Dirichlet condition $d = 0$ is imposed on both edges of the bar such that the localization band can forms at any interior position. In the simulation, no *ad hoc* imperfection is introduced. Note that if the strain/stress fields are strictly uniform everywhere as theoretically predicted, it is impossible to trigger the damage without introducing an imperfection for this example with no elastic singularities. However, mesh bias and numerical errors always exist such that the strain/stress fields are non-uniform.

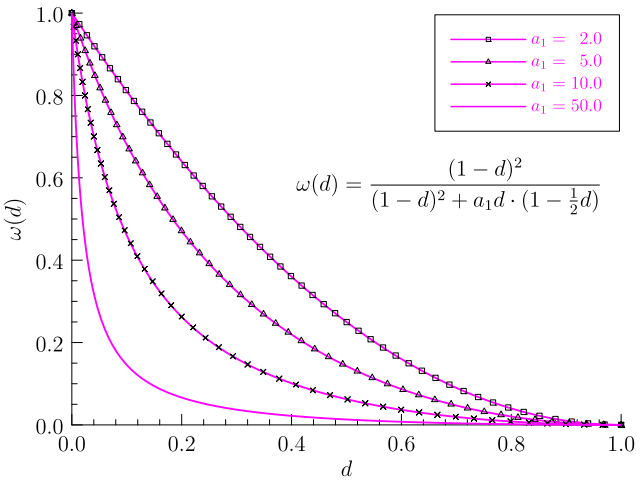


(a) Energetic degradation function (2.38b) for various parameter $a_1$

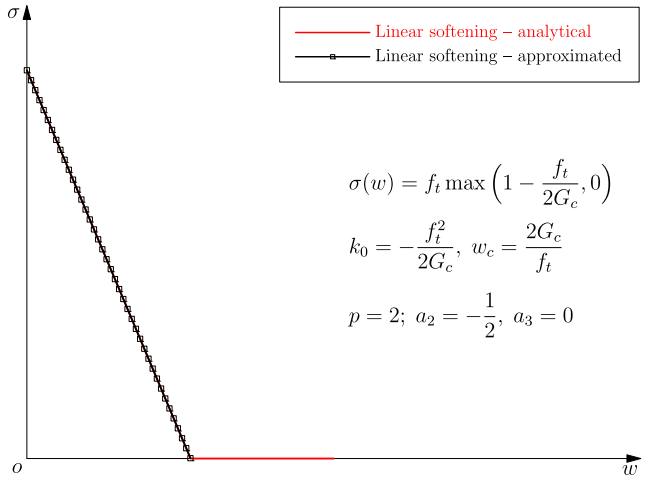


(b) Linear softening curve

**Fig. 3.** Optimal energetic degradation function and the resulting linear softening curve. Though a larger value of parameter $a_1$s result in a more rapidly decreasing $\omega(d)$, the resulting softening curve $\sigma(w)$ is coincident with the expected linear one.


**Fig. 4.** Uniaxial traction of a softening bar: Geometry, boundary and loading conditions.

*3.1.1. Length scale dependent responses given by the classical model*

Let us first consider the gradient-damage model proposed in Pham et al. (2011a) for brittle fracture. The predicted crack patterns at the displacement $u^* = 0.5$ mm are shown in Figs. 5. As expected, the crack bandwidth decreases proportionally with respect to the length scale parameter.

In Fig. 6(a) the numerical curves of load $F^*$ *versus* displacement $u^*$ are depicted. As can be seen, the peak load depends on the length scale parameter. Not surprisingly, as in other existing phase-field models for brittle fracture the critical stress (or crack nucleation strength) is inversely proportional to the square root of the length scale parameter (Bourdin et al., 2008; Tanné et al., 2018). The strain and surface energies during the deformation process shown in Fig. 6(b) and (c) further consolidate the above conclusion. It is this reason that the existing phase-field models tend to regarding the incorporated


(a) $b = 10$ mm and $h = 1$ mm (b) $b = 5$ mm and $h = 0.5$ mm

**Fig. 5.** Uniaxial traction of a softening bar: Damage profiles given by the Pham et al. (2011a) model.

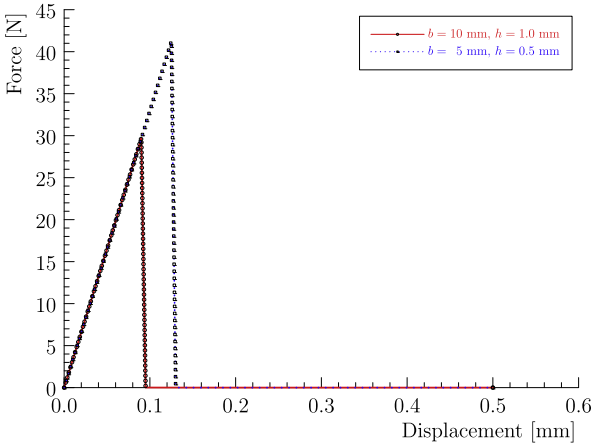


(a) Imposed load

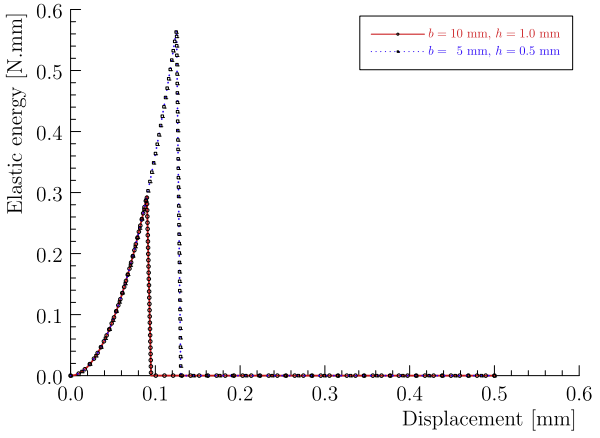


(b) Strain energy

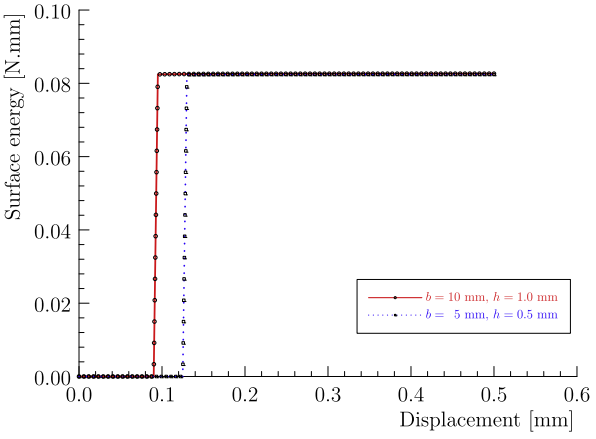


(c) Surface (dissipated) energy

**Fig. 6.** Uniaxial traction of a softening bar: Curves of imposed load and energies *versus* displacement given by the Pham et al. (2011a) model.

length scale as a material property rather than a numerical parameter; see Pham et al. (2011a) and Tanné et al. (2018) among many others. Note that the surface energy is a little bit over-estimated (less than 3%) due to mesh errors, which is consistent with the analytical result derived in Bourdin et al. (2008).

*3.1.2. Length scale independent responses given by the proposed model*

For the proposed model, an extra material parameter, i.e., the failure strength $f_t = 3.0$ MPa, is introduced to match the critical stress predicted by the Pham et al. (2011a) model with the length scale parameter $b = 10$ mm, resulting in an internal length $l_{\text{ch}} = 26.67$ mm.

The predicted damage profiles at the displacement $u^* = 0.5$ mm are shown in Fig. 7. As expected, the crack bandwidth decreases as the length scale parameter $b$ becomes smaller. In Fig. 8 the numerical results of imposed load and of energies *versus* displacement are shown. Obviously, the length scale parameter does not affect the global responses, which is in strong contrast to the existing phase-field damage models for brittle fracture. This property is owing to the optimal characteristic


(a) $b = 10$ mm and $h = 1$ mm (b) $b = 5$ mm and $h = 0.5$ mm

**Fig. 7.** Uniaxial traction of a softening bar: Damage profiles given by the proposed phase-field regularized CZM.

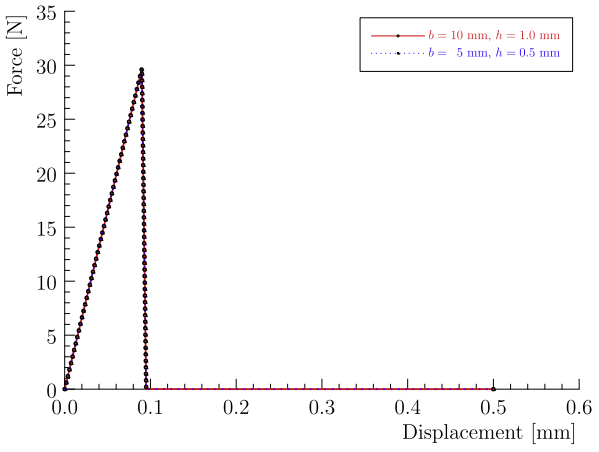


(a) Imposed load

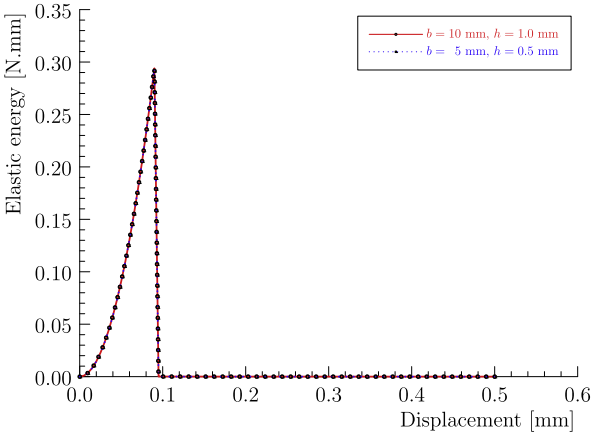


(b) Strain energy

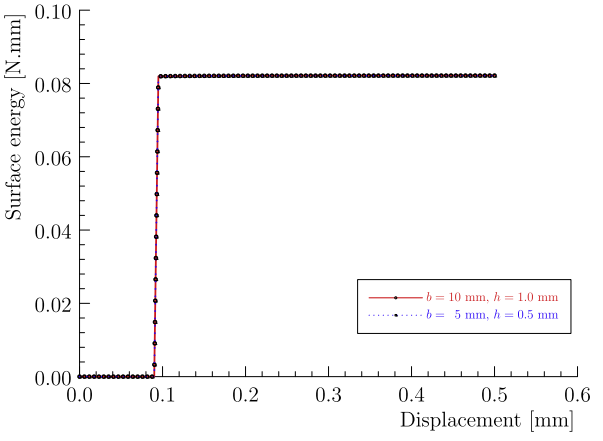


(c) Surface (dissipated) energy

**Fig. 8.** Uniaxial traction of a softening bar: Curves of imposed load and energies *versus* displacement given by the proposed phase-field regularized CZM.

functions, and in particular, to the length scale dependent energetic function, which yield a phase-field regularized CZM. Again, the surface energy is a little bit over-estimated (less than 3%) due to the numerical discretization.

### *3.2. Single-edge notched plate*

Let us now consider the test of a single-edge notched plate. As shown in Fig. 9, it is a square plate of length 1 mm, with unit out-of-plane thickness. A straight horizontal notch of length 0.5 mm is introduced at the mid-height of the left edge. The bottom edge is fixed, while a vertical displacement for the tension test and a horizontal one for the shear one are applied to the top edge, respectively. This example has becomes a popular benchmark test to verify phase-field models for brittle fracture (Ambati et al., 2015; Miehe et al., 2010a).

The following material parameters are adopted: Young's modulus $E_0 = 2.1 \times 10^5$ MPa, Poisson's ratio $\nu_0 = 0.3$, the failure strength $f_t = 2445.42$ MPa, the fracture toughness $G_f = 2.7$ N/mm, resulting in an internal length $l_{ch} = 0.095$ mm. The above

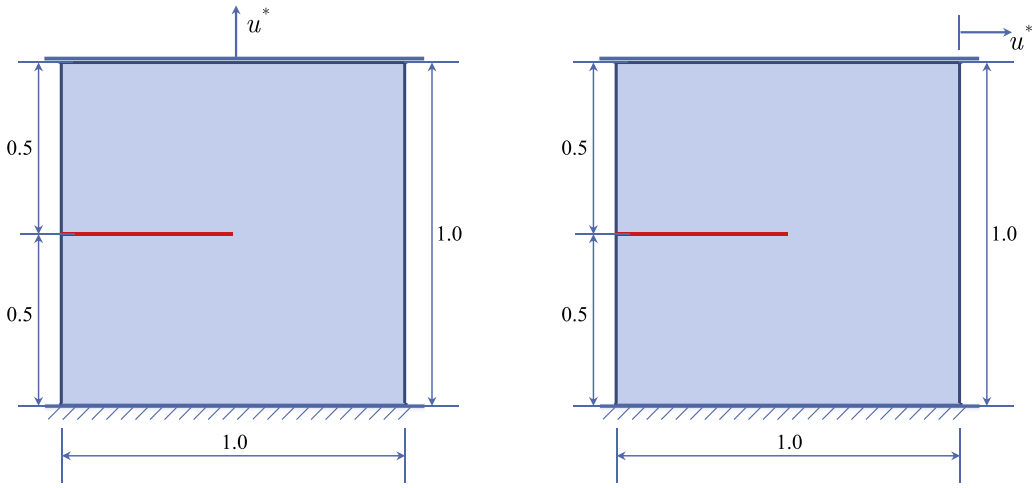


(a) Tension test (b) Shear test

**Fig. 9.** Single-edge notched plate: Geometry (unit of length: mm), boundary and loading conditions.

failure strength is adopted to match the critical stress given by the standard phase-field model (Bourdin et al., 2000; 2008) with a length scale parameter $b = 0.015$ m; see Ambati et al. (2015); Miehe et al. (2010a). In the numerical simulation, two length scale parameters, i.e., $b = 0.01$ mm and $b = 0.005$ mm, are considered. In each case, the mesh size is adopted as $h = b/5$ such that the non-uniform damage field of high gradient within the localization band is well resolved. For this example, the initial crack surface $A = 0.5$ mm$^2$ is approximated with high precision by the regularized one $A_d = 0.5047$ mm$^2$ for $b = 0.01$ mm and $A_d = 0.5031$ mm$^2$ for $b = 0.005$ mm, respectively (Wu, 2017). The initial notch is modeled by the discretized mesh, though it can also be considered by the Dirichlet boundary condition $d(\boldsymbol{x}) = 1$ applied to those nodes on the initial notch.

*3.2.1. Tension test*

The tension test is first discussed. Fig. 10 depicts the crack patterns at displacement $u^* = 0.006$ mm. For both values of the length scale parameter, the crack propagates horizontally to the right edge. As expected, the crack bandwidth is affected by (proportional to) the length scale parameter. The predicted curves of load *versus* displacement are shown in Fig. 11. Remarkably, the numerical global responses are independent of the length scale parameter. This property is attributed, on the one hand, to sufficient resolution of the sharp crack topology approximated by the phase-field regularized counterpart, and on the other hand, to the adopted characteristic functions, both of which result in a phase-field regularized CZM with linear softening.

*3.2.2. Shear test*

For the shear test, the predicted crack patterns at displacement $u^* = 0.02$ mm are shown in Fig. 12. Similarly to those presented in the literature (Ambati et al., 2015; Miehe et al., 2010a), the crack nucleates at the pre-notch tip and propagates downward to the right bottom corner. The length scale parameter affects only the crack bandwidth, but the crack pattern is not influenced. The numerical curves of load *versus* displacement are depicted in Fig. 13 which are consistent with those presented in the literature (Ambati et al., 2015; Miehe et al., 2010b).

As can be seen, the post-peak behavior softens initially until no further damage evolution around the lower-right corner is possible. The cracked specimen is then clamped at the undamaged lower-right portion of the boundary and the force increases again. Remarkably, the length scale parameter has negligible influences on the global responses.

*3.3. Symmetrically notched beam under three-point bending*

The third example concerns a symmetrically notched beam under three-point bending. As shown in Fig. 14, the beam is of span 8 mm, of height 2 mm and of out-of-plane thickness 1 mm. A triangular notch of size 0.2 mm $\times$ 0.4 mm is introduced at the middle of the bottom surface. This example has been widely employed to verify phase-field models for brittle fracture (Ambati et al., 2015; Miehe et al., 2010a).

The material parameters are taken as: Young's modulus $E_0 = 2.08 \times 10^4$ MPa, Poisson's ratio $\nu_0 = 0.3$, the fracture toughness $G_{\mathrm{f}} = 0.54 \times 10^{-3}$ J/m$^2$ and the failure strength $f_t = 200$ MPa, resulting in an internal characteristic length $l_{\mathrm{ch}} = 0.28$ mm. The above failure strength is adopted to match the critical stress given by the standard phase-field model (Bourdin et al., 2000; 2008) with the length scale parameter $b = 0.03$ m; see Ambati et al. (2015); Miehe et al. (2010a). Two length

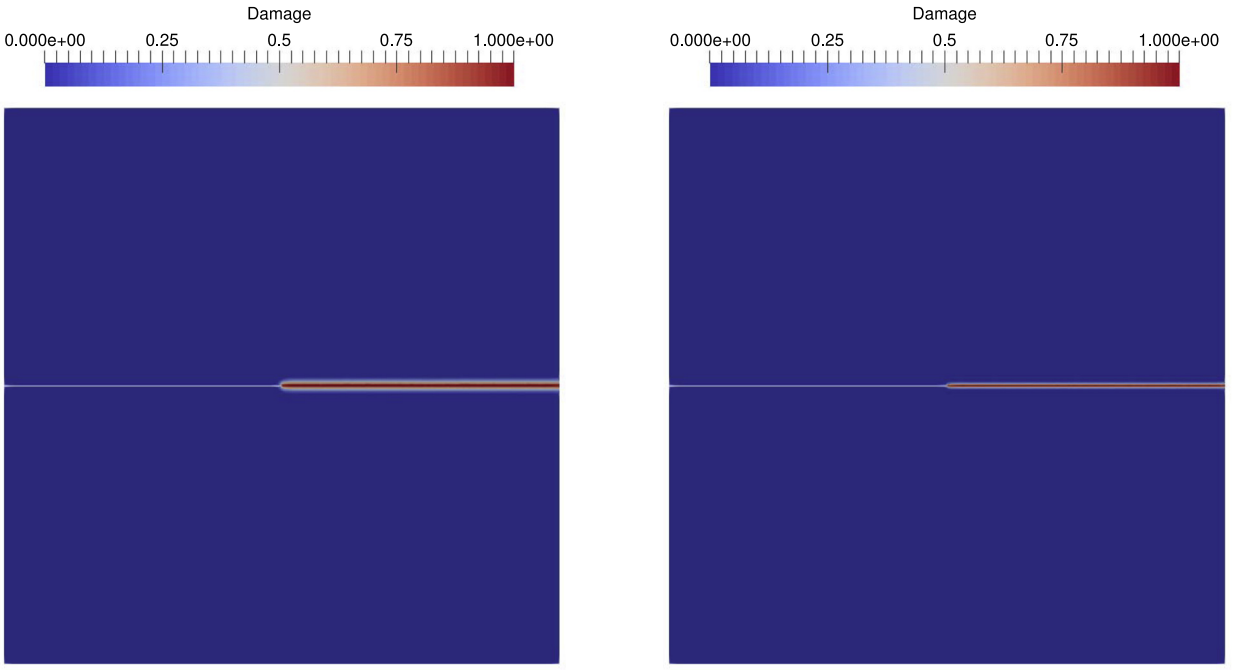


(a) $b = 0.010$ mm and $h = 0.002$ mm (b) $b = 0.005$ mm and $h = 0.001$ mm

**Fig. 10.** Single-edge notched plate under tension: Damage profiles at displacement $u^* = 0.006$ mm.

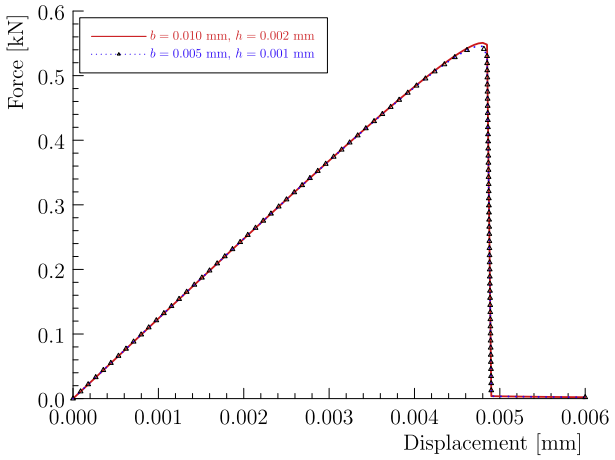


**Fig. 11.** Single-edge notched plate under tension: Load *versus* displacement curves.

scale parameters, $b = 0.02$ mm and $b = 0.01$ mm, are considered with a single mesh size $h = 0.002$ mm, resulting in the ratio $b/h = 10$ and $b/h = 5$, respectively. The crack mouth opening displacement (CMOD) is used to track the unstable post-peak behavior.

The damage profiles at displacement $u^* = 0.08$ mm predicted from the proposed models are shown in Fig. 15. As expected, a crack nucleates at the notch tip and propagates vertically to the top surface of the beam. The length scale parameter only affects the crack bandwidth, but the crack pattern is not affected at all. The load *versus* displacement curves depicted in Fig. 16 shows again that the global responses are insensitive to the length scale.

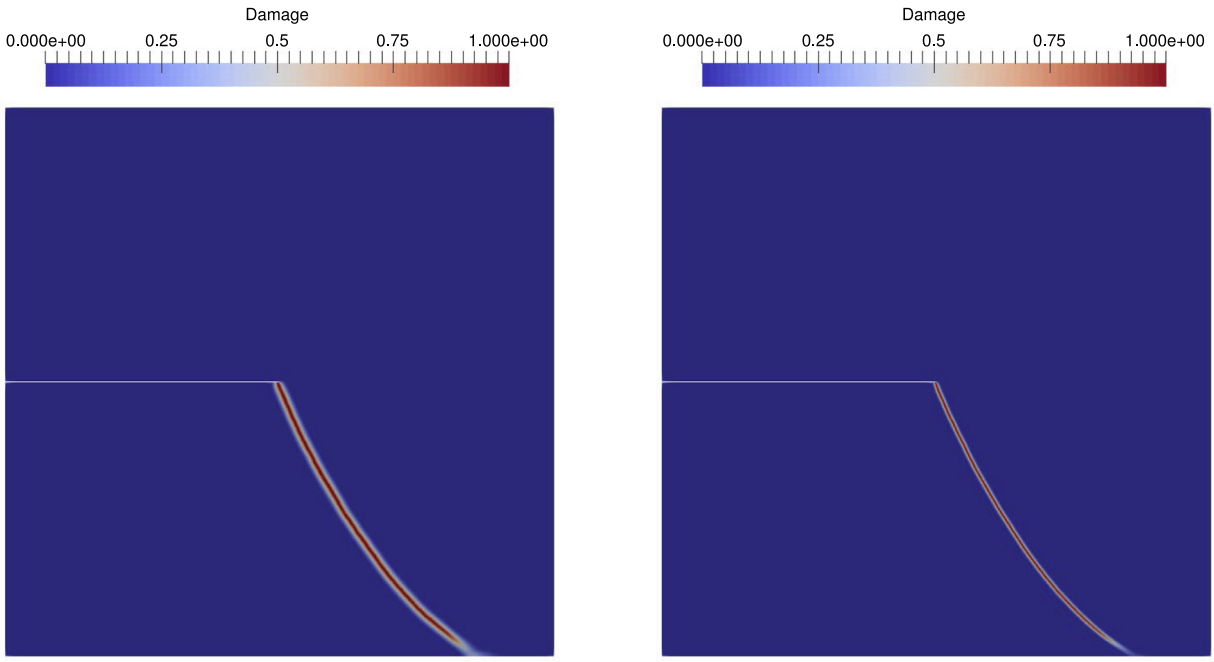


(a) $b = 0.010$ mm and $h = 0.002$ mm (b) $b = 0.005$ mm and $h = 0.001$ mm

**Fig. 12.** Single-edge notched plate under shear: Damage profiles at displacement $u^* = 0.02$ mm.

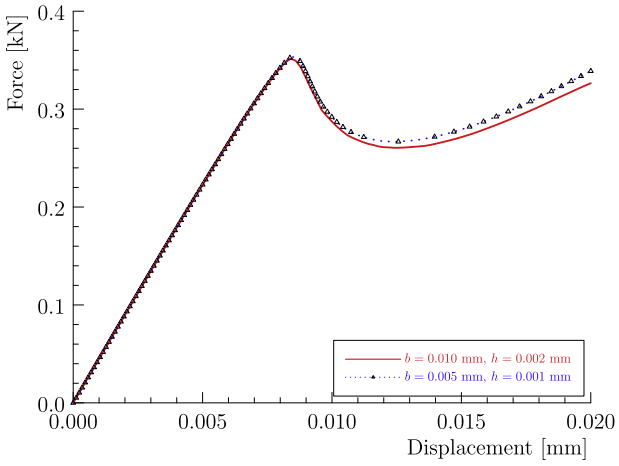


**Fig. 13.** Single-edge notched plate under shear: Load *versus* displacement curves.

### 3.4. Asymmetrically notched beam under three-point bending

Finally, let us consider a set of asymmetrically notched beams under three-point bending. The test was performed by Ingraffea and Grigoriu (1990) and numerically analyzed in Bittencourt et al. (1996). The setup of the problem is shown in Fig. 17.

Various specimen configurations were considered in the test to investigate the influences of the relative locations between the holes and notch, characterized by the values $e_1$ and $e_2$, on the crack pattern and on the global responses. It was found that the observed crack patterns were sensitive to the notch location. For instance, the two specimens with $e_1 = 5.0$ inch and $e_1 = 4.75$ inch (with identical $e_2 = 1.5$ inch) exhibits distinct crack patterns though there was only a subtle difference (less than 2% of the beam span in these two cases) in the value of $e_1$. It is this reason that Ingraffea and Grigoriu (1990) used a probabilistic fracture model to capture the observed crack patterns. To the best knowledge of the authors,

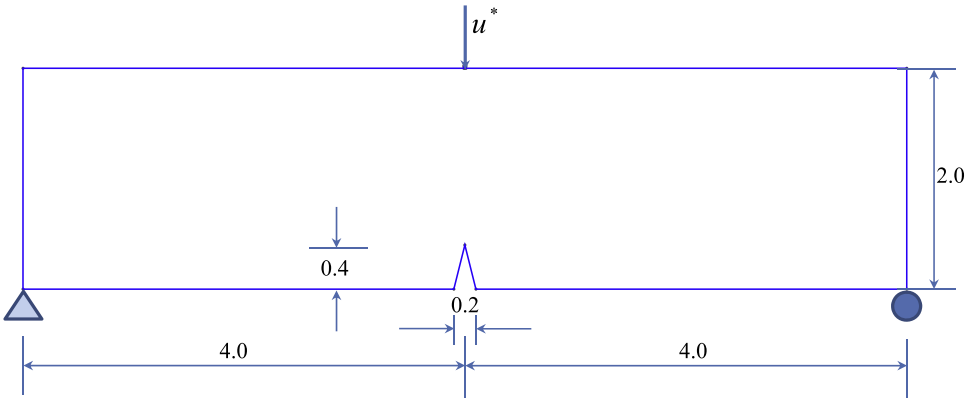


**Fig. 14.** Symmetric notched beam under three-point bending: Geometry (unit of length: mm), loading and boundary conditions.

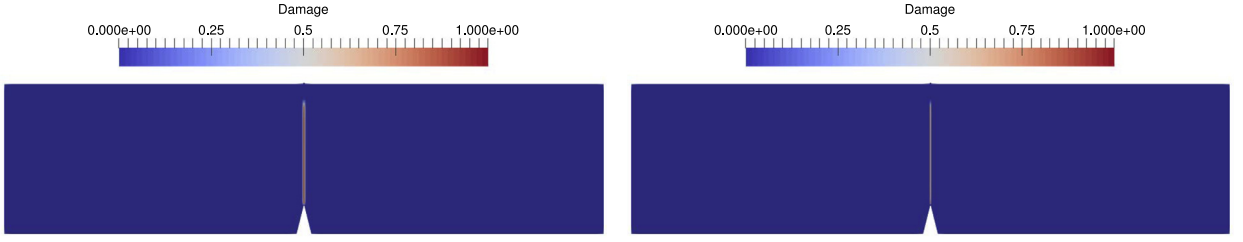


(a) $b = 0.02$ mm and $h = 0.002$ mm (b) $b = 0.01$ mm and $h = 0.002$ mm

**Fig. 15.** Symmetric notched beam under three-point bending: Damage profiles at displacement $u^* = 0.08$ mm given by the proposed model.

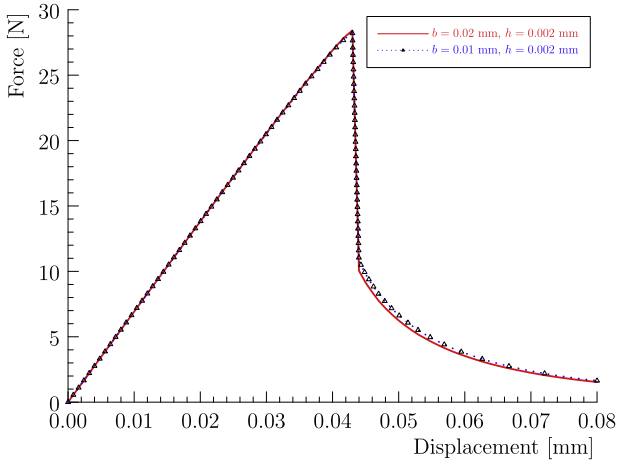


**Fig. 16.** Symmetric notched beam under three-point bending: Curve of load *versus* displacement given by the proposed model.

the experimentally observed crack pattern for the specimen $e_1 = 5.0$ inch and $e_2 = 1.5$ inch has never been reproduced by a continuous (smeared) approach including phase-field models. In this work, the following four cases are considered:

- Specimen (0): a beam with no holes but with a pre-notch of distance $e_1 = 6$ inch and of length $e_2 = 1$ inch;
- Specimen (a): a pre-notched beam identical to Specimen (0), i.e., $e_1 = 6$ inch and $e_2 = 1$, but with three holes;
- Specimen (b): a beam with three holes and a pre-notch defined by $e_1 = 5.15$ inch and $e_2 = 1.5$ inch;
- Specimen (c): a beam with three holes and a pre-notch defined by $e_1 = 4.75$ inch and $e_2 = 1.5$ inch.

Regarding Specimen (0), Ingraffea and Grigoriu (1990) reported the load *versus* CMOD and load *versus* displacement (measured at the loaded point) data, which can be used to calibrate the material parameters. Specimen (a) has been frequently employed in the literature to validate various fracture models and numerical methods; see Ambati et al. (2015); Miehe et al. (2010a) and Mesgarnejad et al. (2015) among many others in the context of phase-field models. Speci-

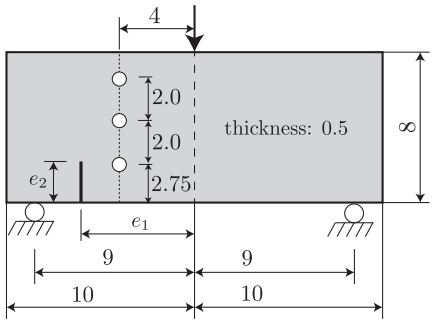


**Fig. 17.** Asymmetrically notched beams under three-point bending: Geometry (unit of length: inch), loading and boundary conditions. The notch's width is 0.05 inch.

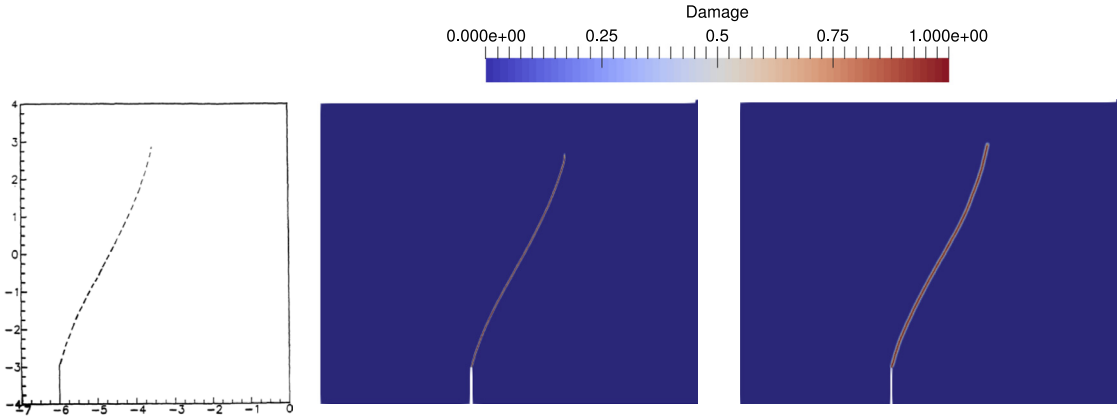


(a) Crack patterns

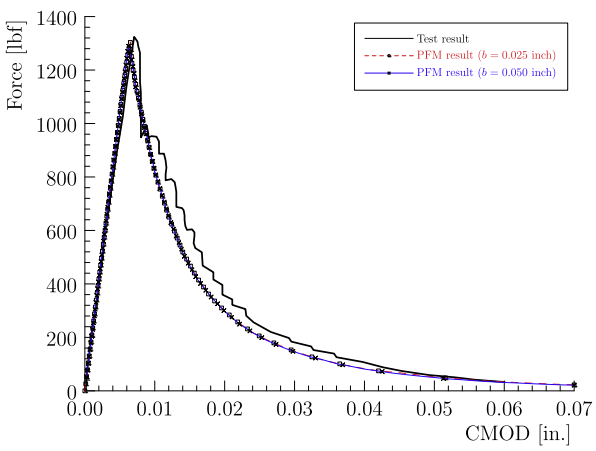


(b) Curve of load *versus* CMOD

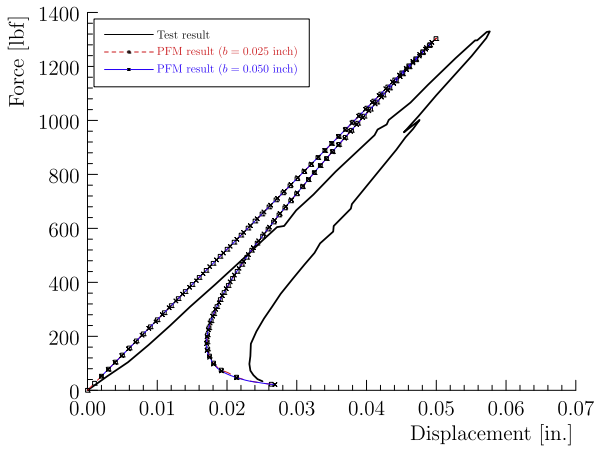


(c) Curve of load *versus* displacement

**Fig. 18.** Asymmetrically notched beam under three-point bending: Numerical results for Specimen (0) with no holes.

men (c) was considered in Cervera et al. (2017) using a local damage model (regualarized by the crack band method) in the context of the stabilized mixed FEM (Cervera et al., 2011). Specimen (b) introduces a negligible difference (less than 1% of the beam span) in the value of $e_1$, mimicking the experimentally tested specimen with $e_1 = 5.0$ inch and $e_2 = 1.5$ inch.

In the numerical simulations, the material parameters are taken from Ingraffea and Grigoriu (1990): Young's modulus $E_0 = 4.75 \times 10^5$ psi ($3.275 \times 10^3$ MPa), Poisson's ratio $\nu_0 = 0.35$, the fracture energy $G_f = 1.8$ lbf/in (315 J/m$^2$) and the failure strength $f_t = 2500$ psi (17.23 MPa), resulting into an internal length $l_{ch} = 0.137$ inch. Two length scale parameters i.e.,

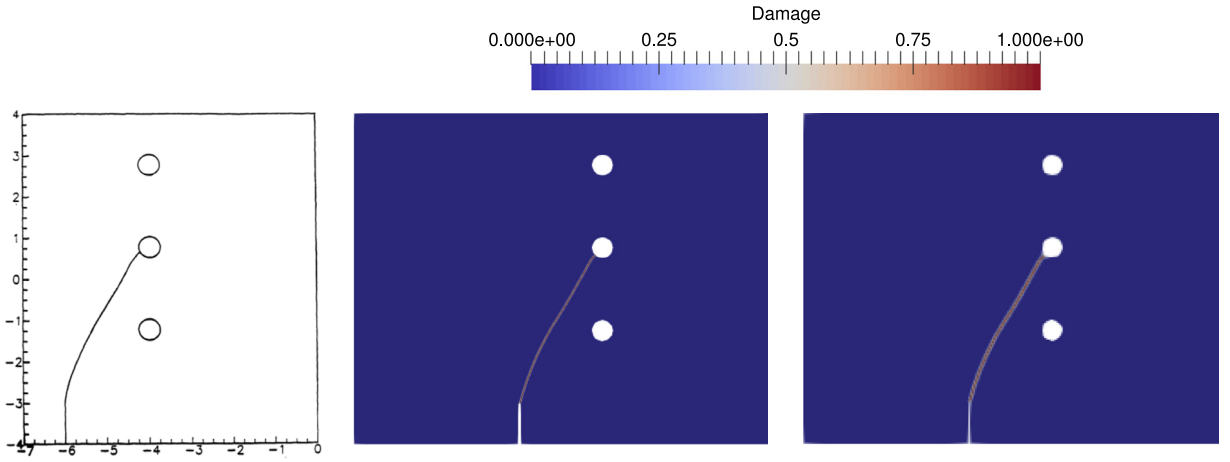


(a) Specimen (a) with $e_1 = 6$ inch and $e_2 = 1$ inch

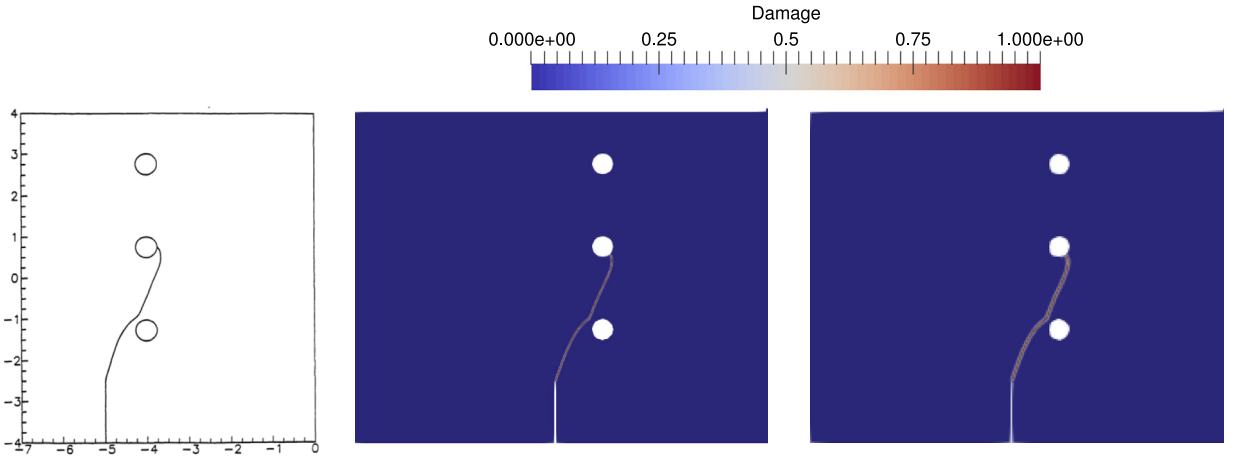


(b) Specimen (b) with $e_1 = 5.15$ inch and $e_2 = 1.5$ inch

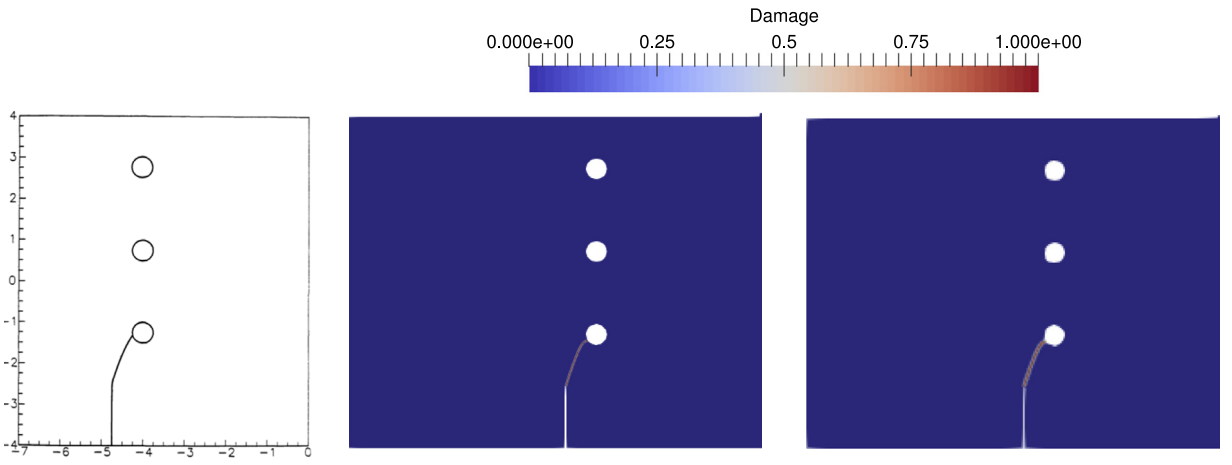


(c) Specimen (c) with $e_1 = 4.75$ inch and $e_2 = 1.5$ inch

**Fig. 19.** Asymmetrically notched beam under three-point bending: Comparison of the crack patterns (Left: experimentally observed crack patterns; Middle: numerically predicted crack patterns with $b = 0.025$ inch; Right: numerically predicted crack patterns with $b = 0.05$ inch).

$b = 0.025$ inch and $b = 0.050$ inch, respectively, are employed together with a single mesh size $h = 0.005$ inch. In order to track the complete failure process in case of snap-backs, the CMOD based indirect displacement control is employed.

Let us first consider Specimen (0) with no holes. The numerically obtained crack pattern at CMOD = 0.07 inch is depicted in Fig. 19(a). The experimentally observed crack path is well captured by the proposed model with two different length scale parameters. The numerical load *versus* CMOD and displacement are shown in Fig. 18(b) and (c), respectively. Not only the peak load but also the post-peak responses agree with the experimental results fairly well . The agreement validates the proposed model for this example of mixed-mode brittle fracture. Again, the incorporated length scale does not affect the global responses at all.

The same material parameters are then adopted for the other three cases. As the test results of global responses are not available, only the influence of the holes on the crack patterns are investigated. The numerical crack pattern of Specimen (a) is compared against the experimental one in Fig. 19(a). The agreement is rather good and remarkably, the subtle fluctuation caused by the local stress concentration around the bottom hole is reproduced. As shown in Fig. 19(b), when the pre-notch is getting closer to the bottom hole as in Specimen (b), fluctuations of the crack path become more pronounced around the bottom hole. If the in-between distance is not close enough, the crack bypasses the bottom hole, continues propagating upwards and eventually reaches the right hand of the middle hole. When the in-between distance is close enough as in Specimen (c) the crack propagating upwards is attracted and then arrested by the bottom hole as shown in Fig. 19(c), though eventually another crack nucleates at the opposite side and propagates upwards (not shown here). The above results are consistent with the experimental observations, validating the proposed model in predicting complex fracture behavior of brittle solids. As expected, the incorporated length scale only affect the crack bandwidth while the crack patterns are not influenced at all.

## 4. Conclusions

Within the framework of our recently proposed unified phase-field damage theory for cohesive fracture, this paper further addresses a length scale insensitive phase-field damage model for brittle fracture. It is motivated from Barenblatt's approximation of Griffith's brittle fracture with a vanishing Irwin's length. More specifically, with the help of a set of optimal characteristic functions, a phase-field based cohesive zone model (CZM) with linear softening law is presented. In particular, both the predicted failure strength and traction – separation law are independent of the incorporated length scale parameter.

Compared to the existing phase-field models and Barenblatt's CZM for brittle fracture, the proposed model is of several advantages. On the one hand, it does not need the cumbersome crack tracking and the elastic penalty stiffness which are both necessary for the CZM based discontinuous approaches. On the other hand, it gives length scale independent global responses while preserving the expected $\Gamma$-convergence property of phase-field models. The above properties, validated by representative numerical examples of well-known benchmark tests, make the proposed model promising for the modeling of brittle fracture.

Several extensions can be made regarding the presented model. Firstly, the same idea may also apply to mode-II fracture. In this respect, besides a different crack driving force, it is crucial to obtain the analytical solution for mode-II fracture and to establish the correspondence to the CZM such that the involved model parameters can be calibrated. Secondly, in phase-field models the localization bandwidth is proportional to the length scale parameter. Accordingly, provided the localization bandwidth is measured from the experiment (e.g., by the digital image correlation technique), the length scale parameter can thus be consistently determined. This strategy can be employed in the presented model since the length scale parameter so determined does not affect the global response. Certainly, both topics need to be elaborated in the future.

## Acknowledgments

This work is supported by the National Key R&D Program of China (2017YFC0803300) and the National Natural Science Foundation of China (51678246) to the first author (J.Y. Wu). The second author (V.P. Nguyen) thanks the funding support from the Australian Research Council via DECRA project DE160100577. Partial support from the State Key Laboratory of Subtropical Building Science (2018ZC04) and the Scientific/Technological Project of Guangzhou (201607020005) to the first author (J.Y. Wu) is also acknowledged.

## Appendix A. Characteristics of the phase-field regularized traction – separation law (2.26)

Regarding the parametrized softening curve (2.26), the initial slope $k_0$ and the ultimate jump $w_c$ with vanishing stresses are determined as (Wu, 2017)

$$k_0 := \lim_{d*\to 0} \frac{\partial \sigma}{\partial w} = -\frac{c_0}{4\pi \xi^2} \frac{\sigma_c^2}{G_f} \left[ \xi \left( a_2 + p + 1 \right) - 1 \right]^{3/2} \tag{A.1a}$$

$$w_c := \lim_{d^*\to 1} w(d^*) = \begin{cases} +\infty & p > 2 \\ \dfrac{2\pi G_{\mathrm{f}}}{c_0\sigma_c}\sqrt{\xi P(1)} & p = 2 \end{cases} \tag{A.1b}$$

for the value $P(1) = 1 + a_2 + a_2a_3 + \ldots$ of the polynomial function $P(d)$ evaluated at $d^* = 1$. Accordingly, for a given traction–separation law $\sigma(w)$ to be approximated, the parameters $a_2$ and $a_3$ in the quadratic polynomial $P(d)$ can be calibrated as

$$a_2 = \frac{1}{\xi}\left[\left(-\frac{4\pi\xi^2}{c_0}\frac{G_{\mathrm{f}}}{f_t^2}k_0\right)^{2/3} + 1\right] - \left(p+1\right) \tag{A.2a}$$

$$a_3 = \begin{cases} 0 & p > 2 \\ \dfrac{1}{a_2}\left[\dfrac{1}{\xi}\left(\dfrac{c_0 w_c f_t}{2\pi G_{\mathrm{f}}}\right)^2 - \left(1+a_2\right)\right] & p = 2 \end{cases} \tag{A.2b}$$

once the parameter $\xi \in (0, 2]$ is determined.

Furthermore, the initial (crack nucleation) and ultimate (completely broken) values of the half bandwidth $D$ of the localization band $\mathcal{B}$, $D_0$ and $D_u$, are given by

$$D_0(\xi, k_0) = \pi b\left[\xi\left(a_2 + p + 1\right) - 1\right]^{-1/2} = b\sqrt[3]{-\frac{c_0\pi^2 f_t^2}{4k_0\xi^2 G_{\mathrm{f}}}} \tag{A.3a}$$

$$D_u(\xi) = \begin{cases} \dfrac{b}{\sqrt{1-\xi}}\ln\left(\dfrac{2\sqrt{1-\xi}+2-\xi}{\xi}\right) & \xi \in (0, 1] \\ \dfrac{b}{\sqrt{\xi-1}}\left(\dfrac{\pi}{2} - \arcsin\dfrac{2-\xi}{\xi}\right) & \xi \in [1, 2] \end{cases} \tag{A.3b}$$

As can be seen, the initial half bandwidth $D_0$ at crack nucleation also depends on the initial slope $k_0$ of the softening curve $\sigma(w)$ as well as on the parameter $\xi \in (0, 2]$.

## Supplementary material

Supplementary material associated with this article can be found, in the online version, at 10.1016/j.jmps.2018.06.006

## References


Ambati, M., Gerasimov, T., de Lorenzis, L., 2015. A review on phase-field models for brittle fracture and a new fast hybrid formulation. Comput. Mech. 55, 383–405.

Ambrosio, L., Tortorelli, V.M., 1990. Approximation of functional depending on jumps by elliptic functional via t-convergence. Commun. Pure Appl. Math. 43 (8), 999–1036.

Amor, H., Marigo, J., Maurini, C., 2009. Regularized formulation of the variational brittle fracture with unilateral contact: numerical experiments. J. Mech. Phys. Solids 57, 1209–1229.

Areias, P., Msekh, M.A., Rabczuk, T., 2016. Damage and fracture algorithm using the screened poisson equation and local remeshing. Eng. Fract. Mech. 158, 116–143.

Areias, P., Rabczuk, T., Msekh, M.A., 2016. Phase-field analysis of finite-strain plates and shells including element subdivision. Comput. Methods Appl. Mech. Eng. 312, 322–350.

Areias, P., Reinoso, J., Camanho, P.P., César de Sá, J., Rabczuk, T., 2018. Effective 2d and 3d crack propagation with local mesh refinement and the screened poisson equation. Eng. Fract. Mech. 189, 339–360.

Balay, S., Abhyankar, S., Adams, M.F., Brown, J., Brune, P., Buschelman, K., Dalcin, L., Eijkhout, V., Gropp, W.D., Kaushik, D., Knepley, M.G., McInnes, L.C., Rupp, K., Smith, B.F., Zampini, S., Zhang, H., Zhang, H., 2016. PETSc Users Manual. Technical Report ANL-95/11 - Revision 3.7. Argonne National Laboratory.

Barenblatt, G.I., 1959. The formation of equilibrium cracks during brittle fracture. general ideas and hypotheses. axially-symmetric cracks. J. Appl. Math. Mech. 23, 622–636.

Bittencourt, T.N., Wawrzynek, P.A., Ingraffea, A.R., Sousa, J.L., 1996. Quasi-automatic simulation of crack propagation for 2d lefm problems. Eng. Fract. Mech. 55 (321–334), 911–944.

de Borst, R., 1987. Computation of post-bifurcation and post-failure behavior of strain-softening solids. Comput. Struct. 25, 211–224.

Bourdin, B., Francfort, G., Marigo, J.-J., 2000. Numerical experiments in revisited brittle fracture. J. Mech. Phys. Solids 48 (4), 797–826.

Bourdin, B., Francfort, G., Marigo, J.-J., 2008. The Variational Approach to Fracture. Springer, Berlin.

Braides, A., 1998. Approximation of Free-Discontinuity Problems. Springer science & Business Media, Berlin.

Carollo, V., Reinoso, J., Paggi, M., 2017. A 3d finite strain model for intralayer and interlayer crack simulation coupling the phase field approach and cohesive zone model. Compos. Struct. 182, 636–651.

Cervera, M., Barbat, G., Chiumenti, M., 2017. Finite element modeling of quasi-brittle cracks in 2d and 3d with enhanced strain accuracy. Comput. Mech. 60 (5), 767–796.

Cervera, M., Chiumenti, M., Codina, R., 2011. Mesh objective modeling of cracks using continuous linear strain and displacement interpolations. Int. J. Numer. Methods Eng. 87 (10), 962–987.

Conti, S., Focardi, M., Iurlano, F., 2015. Phase field approximation of cohesive fracture models. Ann. l'Inst. Henri Poincare (C) Non Linear Anal. 33 (4), 1033–1067.

Cornelissen, H., Hordijk, D., Reinhardt, H., 1986. Experimental determination of crack softening characteristics of normalweight and lightweight concrete. Heron 31 (2), 45–56.
Duflot, M., 2007. A study of the representation of cracks with level sets. Int. J. Numer. Methods Eng. 70, 1261–1302.
Dumstorff, P., Meschke, G., 2007. Crack propagation criteria in the framework of x-fem-based structural analyses. Int. J. Numer. Anal. Methods Geomech. 31, 239–259.
Feng, D.C., Wu, J.Y., 2018. Phase-field regularized cohesize zone model (czm) and size effect of concrete. Eng. Fract. Mech. 197, 66–79.
Focardi, M., Iurlano, F., 2017. Numerical insight of a variational smeared approach to cohesive fracture. J. Mech. Phys. Solids 98, 156–171.
Francfort, G., Marigo, J., 1998. Revisting brittle fracture as an energy minimization problem. J. Mech. Phys. Solids 46 (8), 1319–1342.
Freddi, F., Royer-Carfagni, G., 2010. Regularized variational theories of fracture: a unified approach. J. Mech. Phys. Solids 58, 1154–1174.
Frémond, M., Nedjar, B., 1996. Damage, gradient of damage and principle of virtual power. Int. J. Solids Struct. 33 (8), 1083–1103.
Geuzaine, C., Remacle, J.-F., 2009. Gmsh: a three-dimensional finite element mesh generator with built-in pre- and post-processing facilities. Int. J. Numer. Eng. 79(11), 1309–1331.
Giacomini, A., 2005. Size effects on quasi-static growth of cracks. SIAM J. Math. Anal. 36 (6), 1887–1928.
Griffith, A.A., 1920. The phenomena of rupture and flow in solids. Philos. Trans. R. Soc. London 221, 163–198.
Hillerborg, A., Modéer, M., Petersson, P., 1976. Analysis of crack formation and crack growth in concrete by means of fracture mechanics and finite elements. Cement Concr. Res. 6, 773–781.
Ingraffea, A., Grigoriu, M., 1990. Probabilistic Fracture Mechanics: A Validation of Predictive Capability. Technical Report. DTIC Document
Irwin, G.R., 1957. Analysis of stresses and strains near the end of a crack traversing a plate. J. Appl. Mech. 24, 361–364.
Kuhn, C., Schlüter, A., Müller, R., 2015. On degradation functions in phase field fracture models. Comput. Mater. Sci 108, 374–384.
Lancioni, G., Royer-Carfagni, G., 2009. The variational approach to fracture mechanics. a practical application to the French Panthéon in paris. J. Elast. 95 (1), 1–30.
Lorentz, E., 2017. A nonlocal damage model for plain concrete consistent with cohesive fracture. Int. J. Fract. 207, 123–159.
Lorentz, E., Andrieux, A., 1999. A variational formulation for nonlocal damage models. Int. J. Plast. 15, 119–138.
May, S., Vignollet, J., de Borst, R., 2016. A new arc-length control method based on the rates of the internal and the dissipated energy. Eng. Comput. 33 (1), 100–115.
Mesgarnejad, A., Bourdin, B., Khonsari, M., 2015. Validation simulations for the variational approach to fracture. Comput. Methods Appl. Mech. Engrg. 290, 420–437.
Miehe, C., Hofacker, M., Welschinger, F., 2010. A phase field model for rate-independent crack propagation: robust algorithmic implementation based on operator splits. Comput. Methods Appl. Mech. Eng. 199 (45–48), 2765–2778.
Miehe, C., Schänzel, L., Ulmer, H., 2015. Phase field modeling of fracture in multi-physics problems. part i. balance of crack surface and failure criteria for brittle crack propagation in thermo-elastic solids. Comput. Methods Appl. Mech. Eng. 294, 449–485.
Miehe, C., Welschinger, F., Hofacker, M., 2010. Thermodynamically consistent phase-field models of fracture: variational principles and multi-field fe implementations. Int. J. Numer. Meth. Eng. 83, 1273–1311.
Moës, N., Stolz, C., Bernard, P.-E., Chevaugeon, N., 2011. A level set based model for damage growth: the thick level set approach. Int. J. Numer. Meth. Eng. 86, 358–380.
Msekh, M.A., Cuong, N.H., Zi, G., Areias, P., Zhuang, X., Rabczuk, T., 2018. Fracture properties prediction of clay/epoxy nanocomposites with interphase zones using a phase field model. Eng. Fract. Mech. 188, 287–299.
Mumford, D., Shah, J., 1989. Optimal approximations by piecewise smooth functions and associated variational problems. Commun. Pure Appl. Math. 42 (5), 577–685.
Nguyen, T.T., Yvonnet, J., Bornert, M., Chateau, C., Sab, K., Romani, R., Roy, R.L., 2016. On the choice of parameters in the phase field method for simulating crack initiation with experimental validation. Int. J. Fract. 197, 213–226.
Nguyen, T.T., Yvonnet, J., Zhu, Q.-Z., Bornert, M., Chateau, C., 2016. A phase-field method for computational modeling of interfacial damage interacting with crack propagation in realistic microstructures obtained by microtomography. Comput. Methods Appl. Mech. Eng. 312, 567–595.
Pham, K., Amor, H., Marigo, J.-J., Maurini, C., 2011. Gradient damage models and their use to approximate brittle fracture. Int. J. Damage Mech. 20, 618–652.
Pham, K., Marigo, J.-J., Maurini, C., 2011. The issues of the uniqueness and the stability of the homogeneous response in uniaxial tests with gradient damage models. J. Mech. Phys. Solids 59, 1163–1190.
Pham, K.H., Ravi-Chandar, K., Landis, C.M., 2017. Experimental validation of a phase-field model for fracture. Int. J. Fract. 205, 83–101.
Pijaudier-Cabot, G., Burlion, N., 1996. Damage and localisation in elastic materials with voids. Int. J. Mech. Cohesive Frict. Mater. 1, 129–144.
Reinoso, J., Paggi, M., 2017. Revisiting the problem of a crack impinging on an interface: a modeling framework for the interaction between the phase field approach for brittle fracture and the interface cohesive zone model. Comput. Methods Appl. Mech. Eng. 321, 145–172.
Rice, J.R., 1968. A path independent integral and the approximate analysis of strain cncentrations by notches and cracks. J. Appl. Mech.-T ASME 35, 379–386.
Tanné, E., Li, T., Bourdin, B., Marigo, J.-J., Maurini, C., 2018. Crack nucleation in variational phase-field models of brittle fracture. J. Mech. Phys. Solids 110, 80–99.
Unger, J., Eckardt, S., Könke, C., 2007. Modelling of cohesive crack growth in concrete structures with the extended finite element method. Comput. Methods Appl. Mech. Eng. 196, 4087–4100.
Verhoosel, C.V., de Borst, R., 2013. A phase-field model for cohesive fracture. Int. J. Numer. Methods Eng. 96, 43–62.
Vignollet, J., May, S., de Borst, R., Verhoosel, C.V., 2014. Phase-field model for brittle and cohesive fracture. Meccanica 49, 2587–2601.
Wu, J.Y., 2017. A unified phase-field theory for the mechanics of damage and quasi-brittle failure in solids. J. Mech. Phys. Solids 103, 72–99.
Wu, J.Y., 2018a. A geometrically regularized gradient-damage model with energetic equivalence. Comput. Methods Appl. Mech. Eng. 328, 612–637.
Wu, J.Y., 2018b. Numerical implementation of non-standard phase-field damage models. Comput. Methods Appl. Mech. Eng. in press
Wu, J.Y., Cervera, M., 2018. A novel positive/negative projection in energy norm for the damage modeling of quasi-brittle solids. Int. J. Solids Struct. 139–140, 250–269.
Zhang, X., Sloan, S.W., Vignes, C., Sheng, D., 2017. A modification of the phase-field model for mixed mode crack propagation in rock-like materials. Comput. Methods Appl. Mech. Eng. 322, 123–136.